TITLE PAGE

Increased intrinsic membrane excitability is associated with hypertrophic olivary degeneration in spinocerebellar ataxia type 1

Abbreviated title: Olivary hyperexcitability and HOD in SCA1

Logan M. Morrison[1,2,3], Haoran Huang[4,5], Hillary P. Handler[6], Min Fu[2,3], David D. Bushart[5], Samuel S. Pappas[2,3], Harry T. Orr[7,8], Vikram G. Shakkottai[2,3,*]

Neuroscience Graduate Program[1], University of Michigan, Ann Arbor, MI 48109, USA
Peter O'Donnell Jr. Brain Institute[2], University of Texas Southwestern Medical Center, Dallas, TX 75390, USA
Department of Neurology[3], University of Texas Southwestern Medical Center, Dallas, TX 75390, USA
Medical Scientist Training Program[4], The Ohio State University, Columbus, OH 43210 USA
College of Medicine[5], The Ohio State University, Columbus, OH 43210 USA
Molecular Diagnostics Laboratory[6], University of Minnesota Fairview Medical Center, Minneapolis, MN 55455, USA
Institute for Translational Neuroscience[7] and Department of Laboratory Medicine and Pathology[8], University of Minnesota, Minneapolis, MN 55455, USA

[*]Indicates corresponding author

Corresponding author:
Vikram G. Shakkottai, MD, PhD
Peter O'Donnell Jr. Brain Institute
Department of Neurology and Neurotherapeutics
University of Texas Southwestern Medical Center
NL9.138A, 5323 Harry Hines Blvd,
Dallas, TX 75390
vikram.shakkottai@utsouthwestern.edu

Section outline and figure count
Number of figures: 8
Number of tables or multimedia: 0
Number of extended figures/tables: 1
Abstract word count: 250
Significance statement word count: 119
Introduction word count: 648
Discussion word count: 1499

Conflicts of Interests
The authors declare no competing financial interests.

Acknowledgments

Morrison et al., submitted 2023

Morrison et al., submitted 2023

1 Abstract

2 One of the characteristic areas of brainstem degeneration across multiple spinocerebellar ataxias

3 (SCAs) is the inferior olive (IO), a medullary nucleus that plays a key role in motor learning. In

4 addition to its vulnerability in SCAs, the IO is also susceptible to a distinct pathology known as

5 hypertrophic olivary degeneration (HOD). Clinically, HOD has been exclusively observed after

6 lesions in the brainstem disrupt inhibitory afferents to the IO. Here, for the first time, we describe

7 HOD in another context: spinocerebellar ataxia type 1 (SCA1). Using the genetically-precise

8 SCA1 knock-in mouse model (SCA1-KI; both sexes used), we assessed SCA1-associated changes

9 in IO neuron structure and function. Concurrent with degeneration, we found that SCA1-KI IO

10 neurons are hypertrophic, exhibiting early dendrite lengthening and later somatic expansion.

11 Unlike in previous descriptions of HOD, we observed no clear loss of IO inhibitory innervation;

12 nevertheless, patch-clamp recordings from brainstem slices reveal that SCA1-KI IO neurons are

13 hyperexcitable. Rather than synaptic disinhibition, we identify increases in *intrinsic* membrane

14 excitability as the more likely mechanism underlying this novel SCA1 phenotype. Specifically,

15 transcriptome analysis indicates that SCA1-KI IO hyperexcitability is associated with a reduced

16 medullary expression of ion channels responsible for spike afterhyperpolarization (AHP) in IO

17 neurons – a result that has a functional consequence, as SCA1-KI IO neuron spikes exhibit a

18 diminished AHP. These results reveal membrane excitability as a potential link between disparate

19 causes of IO degeneration, suggesting that HOD can result from any cause, intrinsic or extrinsic,

20 that increases excitability of the IO neuron membrane.

21

22

23

Significance statement

Little is known about the factors that make inferior olive (IO) neurons susceptible to degeneration in the spinocerebellar ataxias (SCAs), a group of inherited neurodegenerative movement disorders. Another well-described form of IO degeneration, known as hypertrophic olivary degeneration (HOD), results from inhibitory denervation of the IO after brainstem injury. Here, we describe a novel finding of HOD in SCA1 without inhibitory denervation, in association with increased intrinsic membrane excitability and reduced potassium channel transcripts. This suggests that increased membrane excitability may be the underlying primary mechanism of HOD. Identifying hyperexcitability as the mechanistic driver of HOD would imply that reducing intrinsic IO excitability could be an effective strategy for treating diverse causes of both inherited and sporadic olivary degeneration.

Introduction

The inferior olive (IO) is a nucleus in the medullary brainstem that plays an important role in cerebellar motor learning (Lang et al., 2017). IO neurons send powerful excitatory projections known as climbing fibers into the cerebellum, where they synapse onto Purkinje cell dendrites to generate cerebellar complex spikes (De Zeeuw et al., 1998; Ausim Azizi, 2007; Ito, 2013; Llinas, 2013). The IO is susceptible to degeneration in a number of conditions, including sporadic olivopontocerebellar atrophy (OPCA) (Konigsmark and Weiner, 1970; Duvoisin, 1984) and the spinocerebellar ataxias (Seidel et al., 2012). In addition, IO neurons are vulnerable to a pathology known as hypertrophic olivary degeneration (HOD). Clinically, HOD occurs secondary to lesions in the brainstem (pontine hemorrhage, most commonly (Smets et al., 2017)) that disrupt inhibitory fibers that travel from the contralateral dentate nucleus of the cerebellum and through the brainstem

47   to synapse onto the IO (a white matter tract known as the Guillain-Mollaret triangle (Ogut et al.,

48   2023)). An acute lesion to these fibers results in an initial increase in IO neuron soma size,

49   generally observed as an increase in gross IO volume (Jellinger, 1973; Ruigrok et al., 1990; Wang

50   et al., 2019). This is ultimately followed by cell loss, gliosis, and atrophy of the IO, a process that

51   sometimes extends for years after the initial insult (Goto and Kaneko, 1981; Pandey et al., 2013).

52   Although HOD ultimately results in IO degeneration, its pathology is considered distinct from the

53   IO atrophy observed in OPCA and the spinocerebellar ataxias due to the lack of any clinically-

54   evident hypertrophy in these disorders (Koeppen, 2018).

55

56   The spinocerebellar ataxias (SCAs) are a group of inherited neurodegenerative diseases that cause

57   a progressive loss of motor function (Paulson, 2009; Seidel et al., 2012). Progressive brainstem

58   degeneration (including in the IO) is known to occur in SCA1, SCA2, SCA3, and SCA7, which

59   together account for the majority of SCA cases (Rub et al., 2013). This pathology manifests late

60   in disease progression, corresponding closely to the onset of breathing and swallowing deficits

61   (symptoms that can eventually cause premature death, especially in SCA1) (Durr, 2010). Among

62   these common SCAs, the fastest-progressing is SCA1 (Scott et al., 2020), a subtype that exhibits

63   IO degeneration as a characteristic pathology (Koeppen et al., 2013). The mechanisms that

64   underlie this degeneration, as well as brainstem pathology in the SCAs broadly, remain poorly

65   understood.

66

67   In this study, we examined IO morphology and physiology in the genetically-precise SCA1 knock-

68   in (SCA1-KI) mouse model. For the first time, we have identified changes consistent with early

69   HOD in a model not of brainstem injury, but of neurodegenerative disease. In neurons of the

70　principal olivary nucleus (IOPr) of SCA1-KI mice, we observed early dendritic hypertrophy

71　followed by late somatic hypertrophy. We found that these morphological changes are concurrent

72　with a loss of immunoreactivity for the calcium-binding protein calbindin. Calbindin loss is

73　characteristic of SCA1 pathology in both IO neurons (Koeppen et al., 2013; Yu et al., 2014) and

74　Purkinje cells (Vig et al., 1998; Koeppen, 2005) and has been used as a surrogate for

75　neurodegeneration in various mouse models of the disease, including SCA1-KI mice (Burright et

76　al., 1995; Watase et al., 2002). Interestingly, structural and functional analyses of IO innervation

77　demonstrate no loss of inhibitory input, suggesting an intrinsic mechanism of HOD in SCA1 that

78　is distinct from the extrinsic mechanism produced by lesions of the brainstem. Using patch-clamp

79　electrophysiology and unbiased transcriptome analysis, we further found that SCA1-KI IO neurons

80　are hyperexcitable, likely due to a reduced expression of ion channel genes – specifically, genes

81　that encode certain calcium and potassium channels that are known to regulate IO neuron intrinsic

82　excitability by mediating spike afterhyperpolarization (AHP) (Llinas and Yarom, 1981b, a).

83　Together, these results reveal intrinsic membrane excitability as a potential link between disparate

84　causes of HOD, suggesting that hyperexcitability from any cause, extrinsic or intrinsic, converges

85　on the same mechanistic pathway of IO degeneration.

86

Materials and Methods

Mouse studies

89　All animal studies were reviewed and approved by the Institutional Animal Care and Use

90　Committee (IACUC) at the institution where they were performed (University of Michigan,

91　University of Texas Southwestern Medical Center, or University of Minnesota) and were

92　conducted in accordance with the United States Public Health Service's Policy on Humane Care

93   and Use of Laboratory Animals. SCA1 knock-in (SCA1-KI) mice (RRID:MGI:3774931), which

94   express an expanded CAG triplet repeat in the endogenous *Atxn1* locus (Watase et al., 2002), were

95   maintained on a C57BL/6 background. SCA1-KI mice were heterozygous for the expanded *Atxn1*

96   allele ($Atxn1^{154Q/2Q}$), with wild-type littermates ($Atxn1^{2Q/2Q}$) used as controls. SCA1 transgenic

97   (SCA1-Tg) mice (RRID:MGI:5518618) overexpress the human *ATXN1* gene with an expanded

98   CAG triplet repeat under the Purkinje cell-specific murine *Pcp2 (L7)* promotesr (Burright et al.,

99   1995) and were maintained on an FVB background (Jackson Labs, RRID:IMSR_JAX:001800).

100   SCA1-Tg mice were homozygous for the transgene ($ATXN1[82Q]^{tg/tg}$), with age/sex-matched

101   wild-type FVB mice used as controls. For both mouse models, studies were performed at either

102   13-15 weeks of age (defined as the "14 week" timepoint) or 29-32 weeks of age (defined as the

103   "30 week" timepoint). Sexes were balanced for all animal studies.

104

105   **Patch-clamp electrophysiology**

106   *Solutions*

107   Artificial cerebrospinal fluid (aCSF) used in these experiments contained: 125 mM NaCl, 3.8 mM

108   KCl, 26 mM $NaHCO_3$, 1.25 mM NaH_2PO_4, 2 mM $CaCl_2$, 1mM $MgCl_2$, and 10 mM glucose. For

109   all recordings, pipettes were filled with internal solution containing: 140 mM K-Gluconate, 4 mM

110   NaCl, 10^{-3} mM $CaCl_2$, 4mM Mg-ATP, 10^{-2} mM EGTA, 10 mM HEPES, at pH 7.3 and osmolarity

111   ~285 mOsm, as described previously for IO recordings (Lefler et al., 2014).

112

113   *Preparation of brain slices for acute electrophysiological recordings*

114   Slices were prepared using the "hot cut" technique (Huang and Uusisaari, 2013). This process,

115   which involves tissue sectioning in standard aCSF at physiological temperatures rather than a

116   sucrose-rich aCSF at near-freezing temperatures, is a recent advancement that has allowed for

117   patch-clamp recordings in brain regions previously deemed inaccessible in adult mice due to their

118   hypersensitivity to slicing-induced damage. This technique has facilitated studies of nuclei never-

119   before investigated in the adult mouse brain, including the inferior olive (Lefler et al., 2014).

120   Briefly, mice were deeply anesthetized by isoflurane inhalation, decapitated, and brains were

121   rapidly removed and submerged in pre-warmed (33°C) aCSF. 300 µm coronal slices were prepared

122   on a VT1200 vibratome (Leica Biosystems, Deer Park, IL) in aCSF held at 32.5°C-34.0°C during

123   sectioning. Slices were then incubated in carbogen-bubbled (95% O_2, 5% CO_2) aCSF at 33°C for

124   45 min. Slices were then stored in carbogen-bubbled aCSF at room temperature (RT) until use.

125   During recording, slices were placed in a recording chamber and continuously perfused with

126   carbogen-bubbled aCSF at 33°C at a flow rate of 2.5 mL/min.

127

128   *Patch-clamp recordings*

129   IO neurons were visually identified for patch-clamp recordings using a 40x water immersion

130   objective and a Nikon Eclipse FN1 upright microscope with infrared differential interference

131   contrast (IR-DIC) optics. Identified cells were visualized using NIS Elements image analysis

132   software (Nikon, Melville, NY). Patch pipettes were pulled to resistances of ~3 MΩ from thin-

133   walled glass capillaries (World Precision Instruments, Cat# 1B120F-4). Importantly, we found that

134   pipette shape had an outsized impact on the success of these difficult recordings; as such, special

135   care was taken to make pipettes with a short taper and a perfectly flat, ~1 µm diameter tip. Data

136   were acquired using a CV-7B headstage amplifier, a Multiclamp 700B amplifier, a Digidata 1440A

137   interface (Axon Instruments, San Jose, CA), and pClamp-10 software (Molecular Devices, San

138   Jose, CA). All data were digitized at 100 kHz. All voltages were corrected for liquid gap junction

139   potential, previously calculated to be 10 mV (Dell'Orco et al., 2015).

140

141   **Purkinje cell *in-vivo* electrophysiology**

142   *Surgical preparation of craniotomy site*

143   *In-vivo* electrophysiological recordings were performed with custom equipment and techniques as

144   described previously (Heiney et al., 2014). Briefly: 14-week-old wild-type and SCA1-KI mice

145   were surgically prepared for recordings one day in advance. Isoflurane anesthesia (dosage 4% for

146   induction, 1.5% for maintenance) was used during all surgical procedures. After a scalp incision,

147   two 0.6 x 0.06" SL flat SS anchor screws (Antrin, Fallbrook, CA) were placed into the skull

148   slightly posterior to bregma. A custom titanium headplate was then affixed to both the skull and

149   the anchor screws with C&B-Metabond (Parkell, Edgewood, NY), and a recording chamber was

150   shaped around the skull above the cerebellum using dental cement (Lang Dental, Wheeling, IL).

151   Two 3 mm craniotomies (centered at -6.2 AP, ±2.1 ML from Bregma) were performed to expose

152   the anterior lobules of each cerebellar hemisphere. Craniotomy sites were protected with Kwik-Sil

153   (World Precision Instruments, Sarasota, FL) until recording.

154

155   *Recording procedure*

156   On the day of recording, animals were secured to the recording platform using the titanium

157   headplate described above. All recordings were performed in awake mice in a single session per

158   mouse, with the total duration of the session limited to 1 hr. After the headplate was attached to

159   the platform, the dental cement recording chamber was filled with sterile PBS and a 2.5-3.5 MΩ

160   tungsten electrode (Thomas Recording, Giessen, Germany) was inserted into one of the

8

161 craniotomy sites to acquire data. The recording electrode was slowly lowered into the cerebellar

162 cortex until Purkinje cells were identified by their characteristic physiology (20-80 Hz simple

163 spikes and the presence of complex spikes). From this point, the electrode was lowered in 10 μm

164 increments until maximum simple spike amplitude was reached. Though electrode placement

165 varied between animals, final electrode depth was typically 2-3 mm from the surface of the brain.

166 Purkinje cell activity was recorded using a DP-301 differential amplifier (Warner Instruments,

167 Holliston, MA), digitized at 100 kHz using a Digidata 1440A interface (Axon Instruments, San

168 Jose, CA), and analyzed using pClamp-10 software (Molecular Devices, San Jose, CA). A

169 minimum of 5 min of activity was recorded per craniotomy site. Recording position in the

170 cerebellar cortex was verified by assessing tissue damage from the recording electrode via Nissl

171 staining.

172

173 *Data analysis*

174 Complex spike frequency was analyzed in 10 Hz high-pass filtered traces, with the criterion for

175 identification that complex spikes must exhibit a voltage higher than the maximum simple spike

176 peak for the entire trace, as described previously (Warnaar et al., 2015). Displayed traces from *in-*

177 *vivo* electrophysiological recordings were first filtered to reduce minor 60 Hz electrical

178 interference, then high-pass filtered at 10 Hz.

179

180 **Cell filling and morphological analysis**

181 *Filling protocol and section preparation*

182 Before patch clamp recordings, Alexa Fluor 488 Succinimidyl Ester (Invitrogen, Cat# A20000)

183 powder was dissolved separately in internal solution at a concentration of 1 mg/mL. Pipette tips

184   were filled with a miniscule amount of standard internal solution so fluorescent dye would not be

185   washed over the tissue when attempting to patch. This was accomplished by placing pipettes

186   upside down (i.e., tip up) in a microcentrifuge tube containing ~20 μL internal solution for ~5 min,

187   which filled the pipette tip by capillary action. From here, pipettes were backfilled with the

188   fluorescent internal solution, allowing cells to be filled with dye while recording. All cells were

189   filled for 15-20 min and confirmed as filled after pipette removal by the presence of intense somatic

190   fluorescence at 40X (as shown in **Fig. 5A, inset**). Only one cell per side was filled on each section

191   to avoid tracing errors from dendrite overlap. In addition, a scalpel was used to make a small notch

192   in the left spinal trigeminal tract of each section to mark its orientation. After filling was complete,

193   free-floating brainstem sections were immediately fixed in 1% PFA for 1 hr at RT, then washed

194   3x in PBS. To avoid crushing the sections during mounting (as patch-clamp slices are much thicker

195   than typical histological sections) a square was drawn on the slide using clear nail polish and

196   allowed to dry immediately before attempting to mount the tissue. Sections were mounted in this

197   square using ProLong Gold Antifade Mountant with DAPI (Cell Signaling Technology, Cat#

198   8961S), with specific attention being paid to the notch in the section to ensure that the surface of

199   the section with the filled cell was mounted against the coverslip, not the slide.

200

201   *Confocal imaging and of filled cells*

202   Sections were imaged using a Nikon C2+ microscope with a 63x oil immersion objective. Imaging

203   of each cell was accomplished by taking multiple z-stack images at the microscope's minimum of

204   0.207 μm between each image of the stack.

205

206

207   *3D reconstruction of cells and morphological analysis*

208   After imaging, 3D reconstructions of cells were generated from z-stack images using the open-

209   source tracing software Vaa3D (Peng et al., 2010; Peng et al., 2014a; Peng et al., 2014b). For each

210   cell, a conservative initial trace was generated automatically by Vaa3D, then manually reviewed

211   and appended to include all visible projections of the neuron. All single-cell morphological

212   calculations were made automatically by Vaa3D, with dendritic tip and bifurcation counts

213   confirmed as accurate by manual review.

214

215   **Immunohistochemistry**

216   *Sample preparation and imaging*

217   Mice were anesthetized under isoflurane inhalation and brains were removed, fixed in 1%

218   paraformaldehyde (PFA) for 1 hour, after which they were placed in 30% sucrose in phosphate-

219   buffered saline (PBS) for 48 hours at 4°C. Brains were then cryo-embedded in a 1:1 mixture of

220   30% sucrose (in PBS) and OCT compound (Fisher Scientific, Cat# 23-730-571) at -80°C for at

221   least 24 hrs. Tissue blocks were sectioned to 20 µm thickness on a CM1850 cryostat (Leica

222   Biosystems, Deer Park, IL). Tissue was permeabilized with 0.4% triton in PBS, then non-specific

223   binding was minimized by blocking with 5% normal goat serum in 0.1% triton in PBS. Primary

224   antibodies (Abs) were incubated in PBS containing 0.1% triton and 2% normal goat serum at 4°C

225   overnight, while secondary Abs were applied for one hour at room temperature in PBS.

226

227   *Antibodies used*

228   To stain for neuronal nuclear protein (NeuN) for stereology (**Figs. 2 & 4**), Rabbit anti-NeuN

229   primary Ab (1:500, Cell Signaling, Cat# 12943, RRID:AB_2630395) and Goat anti-Rabbit IgG

230   (H+L) Alexa Fluor 488-conjugated secondary Ab (1:200; Invitrogen, Cat# A11034,

231   RRID:AB_2576217) were used. To stain for Calbindin (Calb) for stereology (**Figs. 2 & 4**), Mouse

232   anti-Calb primary Ab (1:1000; Sigma Aldrich, Cat# C9848, RRID:AB_476894) and Goat anti-

233   Mouse IgG (H+L) Alexa Fluor 594-conjugated secondary Ab (1:200; Invitrogen, Cat# A11005,

234   RRID:AB_2534073) were used. To stain for glutamate decarboxylase (GAD) for assessment of

235   IO inhibitory innervation (**Figs. 3 & 4**), Rabbit anti-GAD primary Ab (1:500, Sigma-Aldrich, Cat#

236   G5163, RRID:AB_477019) and Goat anti-Rabbit IgG (H+L) Alexa Fluor 594-conjugated

237   secondary Ab (1:200, Invitrogen, Cat# A11012, RRID:AB_2534079) were used. To stain for

238   Calbindin (Calb) for assessment of IO inhibitory terminals (**Figs. 3 & 4**), Mouse anti-Calb primary

239   Ab (1:1000; Sigma Aldrich, Cat# C9848, RRID:AB_476894) and Goat anti-Mouse IgG (H+L)

240   Alexa Fluor 488-conjugated secondary Ab (1:200; Invitrogen, Cat# A11001, RRID:AB_2534069)

241   were used. To stain for small conductance calcium-activated potassium channel 2 (SK2) in IO ion

242   channel studies (**Fig. 7**), Rat anti-SK2 primary Ab (1:200, NeuroMab clone K78/29, Cat# 75-403,

243   RRID:AB_2877597) and Goat anti-Rat IgG (H+L) Alexa Fluor 488-conjugated secondary Ab

244   (1:200, Invitrogen, Cat# A11006, RRID:AB_2534074) were used. To stain for Calbindin (Calb)

245   for IO ion channel studies (**Fig. 7**), Mouse anti-Calb primary Ab (1:1000; Sigma Aldrich, Cat#

246   C9848, RRID:AB_476894) and Goat anti-Mouse IgG (H+L) Alexa Fluor 594-conjugated

247   secondary Ab (1:200; Invitrogen, Cat# A11005, RRID:AB_2534073) were used.

248

249   *Fluorescence intensity measurements*

250   To measure the intensity of GAD staining (**Figs. 3 & 4**), images acquired at 10x magnification

251   were used. Fluorescence intensity analysis was performed using ImageJ. A rectangular box was

252   placed in the IO, specifically in the area of the principal olivary nucleus (IOPr). Mean pixel

253 intensity was measured for each rectangle, which was then used as the raw fluorescence intensity

254 value for each section. Box size was identical in all cases and placed in similar areas of the IOPr

255 between sections. Two sections were imaged per animal and the mean of their fluorescence values

256 were used as the fluorescence intensity for that animal. All tissue processing and imaging was

257 performed at the same session and microscope settings were identical for all acquired images.

258 During imaging and analysis, the experimenter was blind to genotype.

259

260 *Confocal microscopy*

261 Imaging was performed on a Nikon C2+ confocal microscope. Single-plane images were acquired

262 at 63x magnification using an oil-immersion lens, with microscope settings kept constant between

263 all samples under each set of antibodies. Samples were prepared and imaged with the experimenter

264 blind to genotype.

265

266 **Inferior olive stereology**

267 *Cell counts*

268 Estimates for the total number of neurons (NeuN$^+$ cells) in the IO, total number of healthy neurons

269 (NeuN$^+$,Calb$^+$ cells) in the IO, and total IO volume were quantified with an unbiased stereological

270 approach using the optical fractionator probe in Stereoinvestigator (MBF Bioscience, Williston,

271 VT). 30 μm serial coronal sections through the medulla were mounted on slides and co-stained for

272 NeuN and Calbindin as described above. Sections were observed under epifluorescence on a Zeiss

273 Axioimager M2 microscope, where regions of interest were first outlined using a 10x objective

274 lens. 10 sections per brain were analyzed, with a section evaluation interval of 4. Cells within the

275 outlined region were counted using a 63x oil immersion objective, with a ~20 μm counting depth

276   and 1 μm guard zones. A 200 μm x 200 μm counting frame and 50 μm x 50 μm sampling grid

277   were used for all counts, determined effective in pilot studies such that the Gunderson coefficient

278   of error was less than 0.1 for all markers. The top of each stained cell body was the point of

279   reference. The pyramids (py), ventral gigantocellular reticular nucleus (GRN), lateral

280   paragigantocellular nucleus (PGRNl), medial lemniscus (ml), and magnocellular reticular nucleus

281   (MARN) were used as anatomical boundaries for the IO.

282

283   *Cell size measurements*

284   IOPr neuron cell size was quantified by measuring the average soma area (μm^2) for 30-50 cells per

285   animal. Measurements were made concurrent with stereological analysis using the 63x oil

286   immersion objective and the 4-ray nucleator probe in Stereoinvestigator (MBF Bioscience,

287   Williston, VT). Cell size was measured while visualizing cells with NeuN. Analysis was

288   constrained to the principal nucleus of the inferior olive (IOPr), identified by its distinct laminar

289   structure. 200–400 neurons (from 5–8 brains) were measured for each genotype at each timepoint.

290

291   **Transcriptome analysis**

292   *Administration of antisense oligonucleotides (ASOs)*

293   ASO treatment was performed in SCA1-KI and wild-type mice at 5 weeks of age by intracerebro-

294   ventricular (ICV) injection. For these injections, mice were anesthetized with an intraperitoneal

295   (IP) ketamine/xylazine cocktail (100 mg/kg ketamine and 10 mg/kg xylazine). Using a stereotax,

296   the cranium was burr drilled and a Hamilton Neuros Syringe (65460-05) was positioned at the

297   following coordinates: AP, 0.3; ML, 1.0; DV, –2.7 mm from bregma. Injections of 10 μl ASO

298   618353 (50 μg/μl) dissolved in PBS without Ca/Mg (Gibco, 14190) or vehicle were delivered via

299   a micro-syringe pump at 25 nl/s. Immediate postoperative care included subcutaneous delivery of

300   250 μl saline, carprofen (7 mg/kg) and Buprenorphine SR (Zoopharm Pharmacy) (2 mg/kg).

301

302   *RNA isolation and sequencing*

303   Total RNA was isolated from dissected medullae of 28-week-old wild-type vehicle-injected mice

304   (8 samples), 28-week-old SCA1-KI vehicle injected mice (8 samples), and 28-week-old SCA1-KI

305   ASO-injected mice (7 samples) using TRIzol Reagent (Life Technologies) following the

306   manufacturer's protocols. Tissue was homogenized using RNase-Free Disposable Pellet Pestles

307   (Fisher Scientific) in a motorized chuck. For RNA-seq, RNA was further purified to remove any

308   organic carryover using the RNeasy Mini Kit (Qiagen) following the manufacturer's RNA

309   Cleanup protocol. Purified RNA was sent to the University of Minnesota Genomics Center for

310   quality control, including quantification using fluorimetry (RiboGreen assay, Life Technologies),

311   and RNA integrity was assessed with capillary electrophoresis (Agilent BioAnalyzer 2100, Agilent

312   Technologies Inc.), generating an RNA integrity number (RIN). All submitted samples had greater

313   than 1 μg total mass and RINs greater than or equal to 7.9. Library creation was completed using

314   oligo-dT purification of polyadenylated RNA, which was reverse transcribed to create cDNA.

315   cDNA was fragmented, blunt ended, and ligated to barcoded adaptors. Library was size-selected

316   to 320 bp ±5% to produce average inserts of approximately 200 bp, with size distribution validated

317   using capillary electrophoresis and quantified using fluorimetry (PicoGreen, Life Technologies)

318   and qPCR. Libraries were then normalized, pooled, and sequenced on an Illumina HiSeq 2000

319   using a 100-nt paired-end read strategy. Data were stored and maintained on University of

320   Minnesota Supercomputing Institute Servers. Reads were aligned to the mouse reference genome

321   (GRcm38) with hisat2 (Kim et al., 2015) using default parameters for stranded libraries, the hisat2

15

322   GRCm38 index for the genome plus SNPs, and transcripts and using Ensembl's release 87 of the

323   GRCm38 gene annotations. Read counts per gene were summed using featureCounts from the

324   subread package (Liao et al., 2014). Genes less than about 300 bp are too small to be accurately

325   captured in standard RNA-seq library preparations, so they were discarded from downstream

326   analyses. Differential expression analysis was carried out using the R package DESeq2 (Love et

327   al., 2014). Medulla samples were collected and sequenced in two batches, with batch effect

328   corrected for in the differential expression analysis model. Genes with a false discovery rate (FDR)

329   value ≤ 0.05 were considered significant. For both data sets, genes were ranked by $-\log_{10}(P$ value)

330   using differential expression comparison between the wild-type vehicle-injected and SCA1-KI

331   ASO–injected groups, with the sign of the fold change assigned to the ranking metric; i.e., if the

332   fold change was negative, the ranking metric was $-1 \times (-\log_{10}[P$ value]). Statistically significant

333   differentially-expressed genes (DEGs) were identified as all genes with $P < 0.05$ (or $P_{adjusted} <$

334   0.05, where appropriate) and an expression value of either $\log_2$FoldChange < -0.3 or

335    $\log_2$FoldChange > 0.3.

336

337   **Experimental Design and Statistical Analysis**

338   Experimenters were kept blind to genotype for all experiments to avoid biasing results. To prevent

339   variability within experiments, every individual analysis was performed by the same experimenter

340   (e.g., all GAD staining analysis was performed by the same person) and using the same

341   conditions/settings (e.g., all staining for an experiment was done in a single session and analyzed

342   with the same microscope settings) for that experiment's full mouse cohort. Individual statistical

343   tests are described in the figure legends for all data. As this was an exploratory study, the null

344   hypotheses were not prespecified and calculations for statistical power were not performed prior

16

345 to study initiation. It follows from the exploratory nature of the experiments that calculated P

346 values cannot be interpreted as hypothesis testing but only as descriptive. Though formal power

347 analysis was not performed, we estimated sample size based on our (and others') previous work

348 in SCA1 mouse models. Number of individual datapoints and total number of animals for all

349 experiments are reported in figure legends. Statistical analysis was done using Microsoft Excel,

350 Prism 6.0 (GraphPad Software, Boston, MA), and SigmaPlot (Systat Software, Palo Alto, CA),

351 with statistical significance defined as $P < 0.05$. If statistical significance was achieved, we

352 performed post-hoc analysis corresponding to the experiment, as specified, to account for multiple

353 comparisons. All t-tests were two-tailed Student's t-tests, with the level of significance (alpha) set

354 at 0.05. Enrichment of ion channels was calculated using Fisher's exact test, with initial enrichment

355 calculated by comparing ion channel gene proportion amongst DEGs to ion channel gene

356 proportion amongst all genes analyzed (270 potential mouse ion channel transcripts of 30,973 total

357 transcripts assessed) in a 2 x 2 contingency table.

358

Results

360 **Neurons of the principal olivary nucleus in SCA1 mice undergo degenerative hypertrophy**

361 To assess the morphological changes of neurons in the principal olivary nucleus (IOPr) due to

362 SCA1, we filled individual IOPr neurons from coronal brainstem slices of 14-week-old SCA1

363 knock-in (SCA1-KI) mice. This mouse strain was used because it is the most genetically precise

364 model of SCA1, generated by the insertion of 154 CAG repeats into the endogenous *Atxn1* locus.

365 This causes slowly-progressing movement phenotypes that mirror human SCA1: SCA1-KI motor

366 incoordination begins at 5 weeks (Watase et al., 2002), becomes robust by 14 weeks (Bushart et

367 al., 2021), and is severe by 30 weeks (Cvetanovic et al., 2011). Importantly, these mice also model

368 brainstem phenotypes (unlike previous SCA1 mouse models), as they produce mutant ATXN1 in

369 all cell types in which *Atxn1* is endogenously expressed. We filled cells from both SCA1-KI and

370 wild-type littermate controls with a biologically inert fluorescent dye, then imaged them in three

371 dimensions using z-stack confocal microscopy. Using the open-source imaging software suite

372 Vaa3D (Peng et al., 2010; Peng et al., 2014a; Peng et al., 2014b), we generated 3D reconstructions

373 from these z-stacks to measure various parameters of each cell's shape and size.

374

375 Neurons of the IOPr are multipolar, generally described as having a "cloud" of dendrites

376 surrounding the soma in three dimensions (De Zeeuw et al., 1998; Vrieler et al., 2019). At 14

377 weeks, we found that these IOPr dendritic arbors are significantly larger and more complex in

378 SCA1-KI mice than in wild-type controls (**Fig. 1A**). SCA1-KI IOPr neurons have a greater number

379 of dendritic tips and bifurcations (**Fig. 1B-C**), a larger total length of dendrites (**Fig. 1D**), and a

380 significantly higher fractal dimensionality (a measure of the complexity of a three-dimensional

381 object) (**Fig. 1E**). Though this indicates significant hypertrophy of SCA1-IOPr neuron dendrites,

382 we did not observe a change in the total span of the dendritic arbor (**Fig. 1F-H**). Similarly, soma

383 surface area was largely unchanged between genotypes (**Fig. 1I**).

384

385 To investigate SCA1-related phenotypes in the IO as a whole, we quantified IO cell number in 14-

386 week-old (early symptomatic) and 30-week-old (late symptomatic) mice using unbiased

387 stereology. This was performed using brainstem sections co-stained for neuronal nuclear protein

388 (NeuN; a marker of all neurons) and calbindin (Calb). Calb is a well-conserved calcium-binding

389 protein that plays a critical role in calcium buffering in Purkinje cells (Schwaller et al., 2002).

390 Historically, loss of Calb-immunoreactive (Calb^{+}) Purkinje cells has been widely used as a

391 surrogate for Purkinje cell degeneration in SCA mouse models, including models of SCA1

392 (Watase et al., 2002), SCA2 (Hansen et al., 2013), SCA3 (Switonski et al., 2015), and SCA17 (Cui

393 et al., 2017). Mouse IO neurons also exhibit high levels of Calb expression (Yu et al., 2014), and

394 loss of Calb^{+} cells in the IO has similarly been used as an indicator of degeneration in the IO of

395 both ataxic mice (Zanjani et al., 2004) and human SCA patients (Koeppen et al., 2013). Here, we

396 found that 14-week-old SCA1-KI mice exhibit a ~25% loss of Calb^{+} IO neurons (**Fig. 2E**) without

397 a discernible decrease in total cell number (**Fig. 2D**) or mean IO volume (**Fig. 2F**), suggesting the

398 presence of early IO neurodegeneration in these mice. 30-week-old animals also showed no

399 difference in total IO cell number (**Fig. 2K**) or mean IO volume (**Fig. 2M**), though loss of Calb[+]

400 neurons in the SCA1-KI IO was not significant ($P = 0.0658$) at this stage (**Fig. 2L**).

401

402 While performing stereological quantifications on these sections, we also conducted cell size

403 measurements. Focusing solely on the IOPr, we recorded the soma area of 200-400 cells per

404 genotype at each timepoint (**Fig. 2C,J**). At 14 weeks, we found no difference in the average soma

405 area of IOPr neurons between genotypes (**Fig. 2G**), a result that is consistent with soma area

406 measurements from filled cells at 14 weeks (**Fig. 1I**). However, at 30 weeks, IOPr soma areas were

407 ~25% larger on average in SCA1-KI mice compared to wild-types (**Fig. 2N**), indicating significant

408 somatic hypertrophy. These results, along with the morphological changes observed in single IOPr

409 neurons at 14 weeks (**Fig. 1**), suggest an SCA1-associated hypertrophy in IOPr neurons that

410 appears first in dendrites and later in the soma.

411

412 This concurrence of hypertrophy and degeneration is uncommon amongst neuronal disorders.

413 Interestingly, however, the IO is one of the few brain regions in which degenerative hypertrophy

19

414   has been previously described. This phenomenon, known as hypertrophic olivary degeneration

415   (HOD), can occur if brainstem injury (usually pontine hemorrhage (Smets et al., 2017)) causes

416   substantive loss of inhibitory input to the IO (Wang et al., 2019). The degenerative hypertrophy

417   identified here appears strikingly similar to this well-described pathology, suggesting that SCA1-

418   associated IO dysfunction may constitute a novel cause of HOD.

419

420   **Degenerative hypertrophy in SCA1-KI IOPr neurons is cell-autonomous**

421   In order to rule out other potential causes of HOD, we analyzed inhibitory projections to the IOPr

422   in SCA1-KI and wild-type mice at 14 weeks and 30 weeks. Coronal brainstem sections were

423   stained for glutamate decarboxylase (GAD), a marker of GABAergic terminals (**Fig. 3A,C**). At

424   both 14 weeks and 30 weeks, there was no change in the intensity of GAD staining between groups

425   (**Fig. 3B,D**), indicating that inhibitory input to the IOPr remains structurally intact during IO

426   degeneration. To assess whether these inputs are functionally intact, we performed *in-vivo*

427   recordings of cerebellar Purkinje cells (PCs) in awake, head-fixed SCA1-KI and wild-type mice

428   at 14 weeks. The primary output of IO neurons is the complex spike (CS), a characteristic high-

429   amplitude depolarization of the PC membrane that occurs when climbing fibers are activated

430   (Davie et al., 2008; Streng et al., 2018). These CSs can be observed *in-vivo* as distinctly large

431   depolarizing membrane deflections, as shown in our recordings (**Fig. 3E**). During these recordings,

432   we observed significantly fewer CSs in SCA1-KI PCs compared to wild-type PCs (**Fig. 3F**). This

433   suggests that SCA1-KI IOPr neurons are indeed not experiencing a loss of inhibitory tone, as we

434   would expect disinhibition of the IO to cause an increase in final IO output onto PCs (as previously

435   described (Lang et al., 1996)).

436

437   Because SCA1-KI mice express mutant *Atxn1* via its endogenous promoter, ATXN1 function is

438   altered broadly across the SCA1-KI mouse brain. Thus, it is possible that the observed IO

439   degenerative hypertrophy is being influenced by other affected brain regions within the IO circuit.

440   To determine whether *Atxn1* dysfunction outside of the IO is contributing to this degenerative

441   hypertrophy, we assessed cell number, cell size, and the density of inhibitory inputs in SCA1

442   transgenic mice (SCA1-Tg). These mice overexpress the human *ATXN1* gene with an expanded

443   CAG triplet repeat under the murine *Pcp2 (L7)* promoter (Burright et al., 1995). This drives

444   selective expression of polyglutamine-expanded ATXN1 (82 repeats) in cerebellar Purkinje cells,

445   which results in a more severe motor phenotype than observed in SCA1-KI mice. This includes an

446   earlier age-of-onset of motor symptoms, such that the 14 week timepoint is already late in the

447   symptomatic progression of SCA1-Tg mice (Clark et al., 1997). Unbiased stereological

448   quantification reveals that SCA1-Tg mice do not show signs of IO degeneration at 14 weeks,

449   demonstrated by no loss of Calb$^+$ cells (**Fig. 4E**). Interestingly, though, mean IO volume (**Fig. 4F**)

450   and mean NeuN$^+$ cell count (**Fig. 4D**) both exhibited a significant increase in SCA1-Tg mice

451   compared to wild-type littermate controls. IOPr soma size was unchanged between genotypes (**Fig.**

452   **4C,G**), as did IO GAD immunoreactivity (**Fig. 4H,I**), revealing that inhibitory terminals on the

453   SCA1-Tg IO are structurally intact. Based on these results, there does not appear to be a

454   degenerative hypertrophy phenotype in the SCA1-Tg IO.

455

456   HOD has been historically understood as a non-cell-autonomous phenomenon, arising after

457   inhibitory deafferentation of the IO (Duvoisin, 1984; Boesten and Voogd, 1985; de Zeeuw et al.,

458   1990; Ferrer et al., 1994). These results demonstrate that, in the context of SCA1, a similar cellular

459   phenotype can occur in the absence of any change in IO inhibitory tone. Indeed, a non-olivary

460   disruption in the IO circuit, modeled by SCA1-Tg mice, seemed to have no effect on IO neuron

461   size or viability. This reveals that the IO phenotype observed in SCA1-KI mice is likely cell-

462   autonomous, suggesting a novel cause of degenerative hypertrophy separate from any extrinsic

463   source (as in HOD).

464

465   **SCA1-KI IOPr neurons are hyperexcitable**

466   To explore potential intrinsic causes of degenerative hypertrophy in the SCA1 IO, we performed

467   patch-clamp electrophysiology on acute brainstem slices from 14-week-old SCA1-KI mice and

468   wild-type littermate controls (**Fig. 5A**). All recordings were done in the IOPr, which was

469   distinguished by its laminar structure and anatomical position lateral to the midline. The identity

470   of targeted cells was confirmed by the presence of spontaneous subthreshold oscillations (SSTOs),

471   a low-frequency fluctuation in membrane potential that has been well-established as a

472   characteristic feature of IOPr neurons (Llinas and Yarom, 1986; Llinas, 2009; Choi et al., 2010)

473   (**Fig. 5B**). Using a whole-cell current clamp configuration, we observed the spontaneous activity

474   of these neurons for ~100s. Due to the persistence of SSTOs throughout these recordings, resting

475   membrane potential could not be directly calculated; however, an estimate was made by taking the

476   average potential across 10 s of oscillations (**Fig. 5C**). This estimate of resting membrane potential,

477   as well as the average frequency of SSTOs (**Fig. 5D**), was not significantly different between

478   SCA1-KI IOPr neurons and wild-type IOPr neurons. SCA1-KI IOPr neurons did, however, exhibit

479   a decreased average SSTO amplitude (**Fig. 5E**) and spontaneous spike frequency (**Fig. 5F**).

480

481   After recording spontaneous activity in IOPr neurons, we assessed their evoked activity by

482   injecting increasing levels of current in a whole-cell voltage clamp configuration. Preliminary tests

22

483   revealed that holding cells at a slightly hyperpolarized potential (-80 mV) limited most active

484   conductances. This allowed for the injection of current from a stable baseline, free of SSTOs,

485   spontaneous spikes, and other potential confounding activity. From -80 mV, we injected 0-800 pA

486   depolarizing current in repeated 1 second steps, increasing the amount injected by +50 pA with

487   each successive sweep (**Fig. 6B**). This generated the characteristically wide spikes previously

488   described in IOPr neurons, with their distinctive large afterdepolarization (ADP) visible as a

489   protruding "hump" in the repolarizing phase of the spike (Llinas and Yarom, 1981b) (**Fig. 6C**).

490

491   Current injections in the IOPr revealed a novel hyperexcitability phenotype in the SCA1 IO (**Fig.**

492   **6A**). Unlike wild-type IOPr neurons, SCA1-KI IOPr neurons are able to fire repetitively (**Fig. 6D**)

493   in spike trains that increase in frequency with greater injections of current (**Fig. 6E**). Input

494   resistance was unchanged between the two genotypes (**Fig. 6G**), indicating that differences in

495   excitability could not be explained by changes in passive membrane properties. Rather, further

496   analysis of these spikes suggests that the observed SCA1-KI IOPr hyperexcitability may be related

497   to a disruption of currents post-spike. In SCA1-KI mice, the rate at which IOPr membrane potential

498   depolarizes back to baseline from its minimum is nearly two-fold the rate observed in wild-type

499   mice (**Fig. 6F**). This suggests that the membrane potential of SCA1-KI IOPr neurons can more

500   quickly recover from a previous spike and reach threshold again, which may explain how these

501   cells, unlike wild-type IOPr neurons, are able to generate spike trains.

502

503   **Ion channel transcripts are dysregulated in the SCA1-KI medulla**

504   In order to assess potential causes of hyperexcitability in the SCA1-KI IO, we analyzed previously-

505   obtained medullary transcriptome data from SCA1-KI mice treated with antisense oligo-

506   nucleotides (ASOs) to block *Atxn1* expression. After being administered ASOs at 5 weeks of age,

507   these mice demonstrated significant rescue in both motor behavior and brainstem phenotypes.

508   (Friedrich et al., 2018). At 28 weeks, medullary tissue was harvested from both treated and non-

509   treated mice, as well as untreated wild-type littermate controls, and analyzed by RNA-seq.

510   Comparing untreated wild-type and untreated SCA1-KI medullary transcripts revealed significant

511   dysregulation in 1374 genes. Interestingly, 31 ion channel transcripts were present among these

512   baseline differentially-expressed genes (DEGs), representing a 2.79-fold enrichment compared to

513   ion channel representation in the mouse genome. This enrichment is considered significant

514   (Fisher's exact test, $P = 1.41\text{E-}6$), suggesting that disrupted ion channel expression could play a

515   key role in the development of SCA1-KI brainstem phenotypes. Of these 31 candidate genes, 6

516   encode ion channels that influence excitability synaptically ($IC_{synaptic}$), while the remaining 25

517   encode ion channels that influence excitability intrinsically ($IC_{intrinsic}$) (Alexander et al., 2011). For

518   all but one of these channels, medullary transcripts were downregulated in SCA1-KI mice

519   compared to wild-type controls (**Fig. 7A**), a finding that comports with previous studies that report

520   a primarily downregulated DEG population in SCA1 mouse models (Lin et al., 2000;

521   Niewiadomska-Cimicka et al., 2020).

522

523   To further narrow down this list of potential candidates genes, we analyzed data amongst the ASO

524   treatment groups. Of the original 1374 medullary DEGs in SCA1-KI mice, 317 showed significant

525   rescue after ASO treatment. Included among these 317 ASO-rescued DEGs were 10 ion channel

526   genes, all of which encoded $IC_{intrinsic}$ channels (**Fig. 7B**). This constituted a significant 5.26-fold

527   enrichment of $IC_{intrinsic}$ genes compared to $IC_{intrinsic}$ representation in the mouse genome (Fisher's

528   exact test, $P = 3.43\text{E-}5$), suggesting that the loss of ion channels that regulate intrinsic excitability

529   may be an important contributing factor to brainstem dysfunction in SCA1-KI mice. Of the

530     $IC_{intrinsic}$ candidate genes that underwent significant rescue by ASO treatment, the majority (8 of

531   the 10) achieved "complete" rescue; i.e., their expression level after ASO treatment was not

532   significantly different from baseline levels in wild-type mice (**Fig. 7C**). The full medullary

533   transcriptome dataset analyzed here is available in **Table 7-1**, which reports raw reads for all

534   30,973 transcripts assessed in each group, as well as the results of the statistical comparisons

535   between groups used to define DEGs.

536

537   To determine whether this decrease in medullary $IC_{intrinsic}$ transcripts reflects a loss of protein levels

538   in the IO, we immunostained coronal brainstem slices from 30-week-old SCA1-KI and wild-type

539   mice for the channel encoded by *Kcnn2*: small conductance calcium-activated potassium channel

540   2 (SK2) (**Fig. 7D**). Quantification of SK2 staining intensity on IOPr neurons reveals a ~50%

541   reduction in protein levels (**Fig. 7E**). Taken together, these results suggest that downregulation of

542     $IC_{intrinsic}$ genes in the medulla may play a critical role in SCA1 brainstem pathogenesis.

543

Spikes from SCA1-KI IOPr neurons exhibit a diminished AHP

545   In order to assess the functional consequence of $IC_{intrinsic}$ channel loss in the medulla, we recorded

546   from IOPr neurons using patch-clamp electrophysiology in acute brainstem slices. Using the same

547   voltage clamp protocol described above (**Fig. 8A**), increasing levels of current were injected from

548   a holding potential of -80 mV in 1 s steps to generate spikes. AHP depth from each spike generated

549   from 0 to 800 pA current injected was normalized to that spike's threshold and compiled (note:

550   two hyperpolarizing currents, -100 pA and -50 pA, were injected at the beginning of this protocol

551   to allow for input resistance calculations before interference by spike generation). This revealed a

552   significant loss of average AHP depth in SCA1-KI IOPr neurons (**Fig. 8B,C**). To determine

553   whether this phenomenon is also capable of occurring in IOPr neurons at rest, we conducted similar

554   spike analysis experiments, this time generating single spikes from -60 mV (a holding potential

555   close to the estimated resting membrane potential of these cells (**Fig. 5C**)). In the whole-cell

556   voltage clamp configuration, we injected 0-1000 pA depolarizing current in repeated 10 ms steps,

557   increasing the amount injected by +50 pA with each successive sweep (**Fig. 8D**). In this setting,

558   without the presence of spike trains, average AHP depth was again diminished in SCA1-KI IOPr

559   neurons compared to wild-type IOPr neurons (**Fig. 8F**). Previous studies have demonstrated that

560   potassium channels are the primary determinants of AHP size and shape in IOPr neurons. The

561   observed AHP deficit in SCA1-KI IOPr neurons, as well as the enrichment of $IC_{intrinsic}$ genes

562   among ASO-rescued DEGs in the SCA1-KI medulla (7 of which encode potassium channels (**Fig.**

563   **7C**)), connects ion channel loss in the SCA1 brainstem to a potential functional consequence in

564   IOPr hyperexcitability.

565

Discussion

567   Though the IO has long been identified as a characteristic area of SCA1 pathology (Seidel et al.,

568   2012), it is not known what mechanisms drive disease in this cell population. Here, we describe

569   degenerative hypertrophy in SCA1 IOPr neurons, a previously-unknown IO phenotype of the

570   SCA1-KI mouse model. This appears strikingly similar to hypertrophic olivary degeneration

571   (HOD), a pathology caused by the loss of inhibitory afferents to the IO (Ruigrok et al., 1990; Wang

572   et al., 2019). Our results, however, demonstrate that inhibitory innervation to the IO in SCA1-KI

573   mice is both structurally and functionally intact. Though some limited occurrence of HOD in the

574   context of SCA has been previously reported (Yoshii et al., 2017), this study constitutes the first

575   description of a robust HOD-like phenotype in the proven absence of inhibitory deafferentation.

576   This suggests that there is some downstream consequence of synaptic disinhibition, rather than

577   synaptic disinhibition itself, that is both necessary and sufficient to cause HOD.

578

579   HOD, as historically described, is caused by a lesion in the central tegmental tract or superior

580   cerebellar peduncle, consistent with loss of IO innervation from the dentate nucleus of the

581   cerebellum (Sabat et al., 2016; Tilikete and Desestret, 2017). Though IO neurons receive

582   innervation from a variety of brain regions, previous studies have shown that the dentate nucleus

583   supplies the IO with its primary inhibitory input (Fredette and Mugnaini, 1991; Best and Regehr,

584   2009). Importantly, disruption of this dentato-olivary circuit is the sole condition in which HOD

585   has been observed, leading to the current conclusion that HOD is a consequence of IO neurons

586   losing inhibitory tone. Though we found inhibitory afferents to be intact in the SCA1 IO, these

587   neurons still exhibit hyperexcitability, indicating that increased membrane excitability may be

588   HOD's proximal cause; that is, HOD may occur as the result of *any* phenomenon that sufficiently

589   increases IO membrane excitability, be it extrinsic (as in HOD, historically) or intrinsic (as in

590   SCA1).

591

592   One potential explanation for this connection between excitability and cell size is the possibility

593   that, in the SCA1 IO, hypertrophy is acting in opposition to hyperexcitability as a compensatory

594   mechanism. A substantial lengthening of dendrites, as exhibited in SCA1-KI mice at 14 weeks

595   (**Fig. 1**), is likely to enhance dendritic shunting (Blomfield, 1974). If the multiple excitatory signals

596   that the IO receives were sufficiently diluted by shunting through this extra length of dendrite,

597   membrane excitability would, effectively, be decreased. This may explain the reduction in SCA1-

598   KI Purkinje cell complex spike frequency we observed *in-vivo*: i.e., even though synaptic input to

599   the SCA1-KI IO appears intact, shunting could be diminishing the number of excitatory signals

600   that end up reaching the soma and triggering IO output to the cerebellum – a result that would

601   likely cause deficits in motor learning (Lang et al., 2017). This raises the interesting possibility

602   that HOD may be a 'rogue' compensatory mechanism, such that IO hypertrophy helps the cell (by

603   alleviating hyperexcitability) but harms the circuit (by reducing final cellular output). Similarly,

604   previous studies provide evidence that changes in morphology may also be acting as a

605   compensatory mechanism against hyperexcitability in SCA1 Purkinje cells. Prior to atrophy,

606   Purkinje cells in SCA1-Tg mice exhibit a severe firing phenotype caused by increased membrane

607   excitability; however, after the onset of atrophy, there is a partial restoration of firing. This is likely

608   due to changes in channel density on SCA1 Purkinje cell somas. SCA1 Purkinje cells exhibit

609   reduced expression of multiple key ion channel genes, causing a significant decrease in somatic

610   channel density. However, as a result of a decrease in somatic surface area during atrophy, channel

611   density on the soma increases, which appears to partially alleviate the SCA1-Tg Purkinje cell firing

612   phenotype by reducing membrane excitability (Dell'Orco et al., 2015). Though it is unclear how

613   this compensatory effect of atrophy occurs, there is evidence that channel density on the Purkinje

614   cell soma is an important factor in the formation of functional ion channel clusters, especially those

615   that regulate membrane excitability via potassium conductances (Womack et al., 2004; Kaufmann

616   et al., 2009; Indriati et al., 2013). Taken together, these results suggest a close relationship between

617   morphology and excitability in neurons that are selectively vulnerable to SCA1-associated

618   degeneration. In addition, it raises the question of what causal link, if any, exists between the

619   structural and functional pathologies of these neurons.

620

621   Previous research has demonstrated that the mutation that causes SCA1 (an expansion in the

622   polyglutamine-encoding CAG repeat region of the *ATXN1* gene) produces Purkinje cell pathology

623   by disrupting the expression of a host of downstream genes (Lin et al., 2000; Crespo-Barreto et

624   al., 2010). Due to an abnormal interaction between the polyglutamine-expanded ATXN1 protein

625   and Capicua (CIC), a transcriptional repressor, the vast majority of these Purkinje cell genes

626   exhibit decreased expression in SCA1 (Lam et al., 2006; Rousseaux et al., 2018). Ion channel

627   genes, including many that are crucial for maintaining Purkinje cell excitability, are significantly

628   enriched among this group (Bushart et al., 2018; Chopra et al., 2020). Similarly, in this study, we

629   found a significant enrichment of ion channel genes among the medullary DEGs identified in 28-

630   week-old SCA1-KI mice. the majority of which also exhibit decreased expression. Interestingly,

631   cerebellar transcripts from these same 28-week-old SCA1-KI mice reveal that DEGs in the SCA1

632   cerebellum and the SCA1 medulla are indeed similar, but not identical (Friedrich et al., 2018).

633   Between these two tissues, 7 ion channel DEGs are shared: *Cacna1g*, *Gria1*, *Kcna6*, *Kcnc1*,

634   *Kcnk13*, *Kcnn2*, and *Trpc3*, all exhibiting decreased expression in both brain regions. Based on

635   these observations, it appears that the cerebellum and brainstem may share a common mechanism

636   of SCA1 pathology in reduced ion channel expression. This connection might be explained by the

637   shared presence of CIC, which is moderately expressed in both the mouse cerebellum and the

638   mouse IO (Lein et al., 2007). The discrepancies between 28 week SCA1-KI medullary and

639   cerebellar DEGs, as suggested by a recent study (Driessen et al., 2018), may be due to the

640   involvement of transcription factors other than CIC that are also affected by polyglutamine-

641   expanded ATXN1.

642

643   Within the SCA1 brainstem and cerebellum, there appears to be additional convergence that links

644   IO neuron and Purkinje cell pathology, specifically. Previous research has shown that loss of

645   channels in SCA1-KI Purkinje cells causes a firing dysfunction related to an increase in membrane

646   excitability (Dell'Orco et al., 2015; Chopra et al., 2018). This is driven primarily by abnormalities

647   in spike afterhyperpolarization (AHP), which is significantly shallower in SCA1-KI Purkinje cells

648   at 14 weeks (Bushart et al., 2021). SCA1-KI IO neurons, shown by their ability to generate spike

649   trains (**Fig. 6**), also exhibit an increase in membrane excitability that correlates with an observed

650   AHP deficit (**Fig. 8**). This suggests that hyperexcitability caused by a reduction in spike AHP is a

651   phenotype that is shared by both IO neurons and Purkinje cells in SCA1-KI mice.

652

653   Despite differences in their baseline firing properties, AHP dynamics in both Purkinje cells

654   (Edgerton and Reinhart, 2003; Walter et al., 2006) and IO neurons (Llinas and Yarom, 1981b;

655   Lang et al., 1997) appear to be largely governed by the interplay between calcium currents and

656   potassium currents – especially via the conductance of calcium-activated potassium (K_{Ca})

657   channels. Of the channels that are represented in the two groups of 28 week SCA1-KI DEGs, the

658   majority are either calcium or potassium channels. In addition, one of the 7 channel DEGs shared

659   by both the SCA1-KI cerebellar and medullary datasets is *Kcnn2*, which encodes one of only 5

660   K_{Ca} channels expressed in the brain (Alexander et al., 2017). Together, these findings suggest that

661   hyperexcitability due to altered calcium and/or potassium conductances may represent a shared

662   mechanism of dysfunction in SCA1 IO neurons and Purkinje cells.

663

664   Though the relationship between these physiological changes and cell size remains unclear, prior

665   research has demonstrated that firing abnormalities in SCA1-KI Purkinje cells precede

666   degeneration (Hourez et al., 2011). Previous work has shown that addressing this by increasing

667   specific potassium conductances with pharmacological agents can faithfully restore SCA1-KI

668   Purkinje cell firing *in-vitro*. Additionally, chronic treatment of SCA1-KI mice with these same

669   drugs not only improves motor function but, importantly, also slows the atrophy and subsequent

670   degeneration of Purkinje cells (Chopra et al., 2018; Bushart et al., 2021). As such, by

671   demonstrating that a reduction in SCA1-KI Purkinje cell hyperexcitability is sufficient to partially

672   rescue cell size phenotypes, these results suggest that SCA1-associated disruptions of membrane

673   excitability may be an important driver of morphological changes in Purkinje cells. Similarly,

674   though it is not known what specific effect it had on either SCA1-KI IO neuron hyperexcitability

675   or hypertrophy, ASO administration did partially alleviate brainstem phenotypes in these mice

676   (Friedrich et al., 2018). In addition, the enrichment of ion channel genes among the SCA1-KI

677   medullary DEGs rescued by ASOs (**Fig. 7**) suggests that membrane excitability might be one of

678   the cellular features whose restoration is important to this ASO-mediated rescue of brainstem

679   dysfunction. Together, these results indicate that altered membrane excitability may constitute a

680   key driver of SCA1 pathology in the brainstem – including HOD.

681

682

683

684

685

686

687

688

References

689

690   Alexander SP, Mathie A, Peters JA (2011) Guide to Receptors and Channels (GRAC), 5th edition.

691   Br J Pharmacol 164 Suppl 1:S1-324.

692   Alexander SP, Kelly E, Marrion NV, Peters JA, Faccenda E, Harding SD, Pawson AJ, Sharman

693   JL, Southan C, Buneman OP, Cidlowski JA, Christopoulos A, Davenport AP, Fabbro D,

694   Spedding M, Striessnig J, Davies JA, Collaborators C (2017) THE CONCISE GUIDE TO

695   PHARMACOLOGY 2017/18: Overview. Br J Pharmacol 174 Suppl 1:S1-S16. Ion channel

696   list available from www.guidetopharmacology.org.

697   Ausim Azizi S (2007). . . And the olive said to the cerebellum: organization and functional

698   significance of the olivo-cerebellar system. Neuroscientist 13:616-625.

699   Best AR, Regehr WG (2009) Inhibitory regulation of electrically coupled neurons in the inferior

700   olive is mediated by asynchronous release of GABA. Neuron 62:555-565.

701   Blomfield S (1974) Arithmetical operations performed by nerve cells. Brain Res 69:115-124.

702   Boesten AJ, Voogd J (1985) Hypertrophy of neurons in the inferior olive after cerebellar ablations

703   in the cat. Neurosci Lett 61:49-54.

704   Burright EN, Clark HB, Servadio A, Matilla T, Feddersen RM, Yunis WS, Duvick LA, Zoghbi

705   HY, Orr HT (1995) SCA1 transgenic mice: a model for neurodegeneration caused by an

706   expanded CAG trinucleotide repeat. Cell 82:937-948.

707   Bushart DD, Huang H, Man LJ, Morrison LM, Shakkottai VG (2021) A Chlorzoxazone-Baclofen

708   Combination Improves Cerebellar Impairment in Spinocerebellar Ataxia Type 1. Mov

709   Disord 36:622-631.

710   Bushart DD, Chopra R, Singh V, Murphy GG, Wulff H, Shakkottai VG (2018) Targeting

711   potassium channels to treat cerebellar ataxia. Ann Clin Transl Neurol 5:297-314.

712   Choi S, Yu E, Kim D, Urbano FJ, Makarenko V, Shin HS, Llinas RR (2010) Subthreshold

713   membrane potential oscillations in inferior olive neurons are dynamically regulated by

714   P/Q- and T-type calcium channels: a study in mutant mice. J Physiol 588:3031-3043.

715   Chopra R, Bushart DD, Shakkottai VG (2018) Dendritic potassium channel dysfunction may

716   contribute to dendrite degeneration in spinocerebellar ataxia type 1. PLoS One

717   13:e0198040.

718   Chopra R, Bushart DD, Cooper JP, Yellajoshyula D, Morrison LM, Huang H, Handler HP, Man

719   LJ, Dansithong W, Scoles DR, Pulst SM, Orr HT, Shakkottai VG (2020) Altered Capicua

720   expression drives regional Purkinje neuron vulnerability through ion channel gene

721   dysregulation in spinocerebellar ataxia type 1. Hum Mol Genet 29:3249-3265.

722   Clark HB, Burright EN, Yunis WS, Larson S, Wilcox C, Hartman B, Matilla A, Zoghbi HY, Orr

723   HT (1997) Purkinje cell expression of a mutant allele of SCA1 in transgenic mice leads to

724   disparate effects on motor behaviors, followed by a progressive cerebellar dysfunction and

725   histological alterations. J Neurosci 17:7385-7395.

726   Crespo-Barreto J, Fryer JD, Shaw CA, Orr HT, Zoghbi HY (2010) Partial loss of ataxin-1 function

727   contributes to transcriptional dysregulation in spinocerebellar ataxia type 1 pathogenesis.

728   PLoS Genet 6:e1001021.

729   Cui Y, Yang S, Li XJ, Li S (2017) Genetically modified rodent models of SCA17. J Neurosci Res

730   95:1540-1547.

731   Cvetanovic M, Patel JM, Marti HH, Kini AR, Opal P (2011) Vascular endothelial growth factor

732   ameliorates the ataxic phenotype in a mouse model of spinocerebellar ataxia type 1. Nat

733   Med 17:1445-1447.

734   Davie JT, Clark BA, Hausser M (2008) The origin of the complex spike in cerebellar Purkinje

735   cells. J Neurosci 28:7599-7609.

736   de Zeeuw CI, Ruigrok TJ, Schalekamp MP, Boesten AJ, Voogd J (1990) Ultrastructural study of

737   the cat hypertrophic inferior olive following anterograde tracing, immunocytochemistry,

738   and intracellular labeling. Eur J Morphol 28:240-255.

739   De Zeeuw CI, Simpson JI, Hoogenraad CC, Galjart N, Koekkoek SK, Ruigrok TJ (1998)

740   Microcircuitry and function of the inferior olive. Trends Neurosci 21:391-400.

741   Dell'Orco JM, Wasserman AH, Chopra R, Ingram MA, Hu YS, Singh V, Wulff H, Opal P, Orr

742   HT, Shakkottai VG (2015) Neuronal Atrophy Early in Degenerative Ataxia Is a

743   Compensatory Mechanism to Regulate Membrane Excitability. J Neurosci 35:11292-

744   11307.

745   Driessen TM, Lee PJ, Lim J (2018) Molecular pathway analysis towards understanding tissue

746   vulnerability in spinocerebellar ataxia type 1. Elife 7.

747   Durr A (2010) Autosomal dominant cerebellar ataxias: polyglutamine expansions and beyond.

748   Lancet Neurol 9:885-894.

749   Duvoisin RC (1984) An apology and an introduction to the olivopontocerebellar atrophies. Adv

750   Neurol 41:5-12.

751   Edgerton JR, Reinhart PH (2003) Distinct contributions of small and large conductance Ca2+-

752   activated K+ channels to rat Purkinje neuron function. J Physiol 548:53-69.

753   Ferrer I, Genis D, Davalos A, Bernado L, Sant F, Serrano T (1994) The Purkinje cell in

754   olivopontocerebellar atrophy. A Golgi and immunocytochemical study. Neuropathol Appl

755   Neurobiol 20:38-46.

756   Fredette BJ, Mugnaini E (1991) The GABAergic cerebello-olivary projection in the rat. Anat

757   Embryol (Berl) 184:225-243.

758   Friedrich J, Kordasiewicz HB, O'Callaghan B, Handler HP, Wagener C, Duvick L, Swayze EE,

759   Rainwater O, Hofstra B, Benneyworth M, Nichols-Meade T, Yang P, Chen Z, Ortiz JP,

760   Clark HB, Oz G, Larson S, Zoghbi HY, Henzler C, Orr HT (2018) Antisense

761   oligonucleotide-mediated ataxin-1 reduction prolongs survival in SCA1 mice and reveals

762   disease-associated transcriptome profiles. JCI Insight 3.

763   Goto N, Kaneko M (1981) Olivary enlargement: chronological and morphometric analyses. Acta

764   Neuropathol 54:275-282.

765   Hansen ST, Meera P, Otis TS, Pulst SM (2013) Changes in Purkinje cell firing and gene expression

766   precede behavioral pathology in a mouse model of SCA2. Hum Mol Genet 22:271-283.

767   Heiney SA, Kim J, Augustine GJ, Medina JF (2014) Precise control of movement kinematics by

768   optogenetic inhibition of Purkinje cell activity. J Neurosci 34:2321-2330.

769   Hourez R, Servais L, Orduz D, Gall D, Millard I, de Kerchove d'Exaerde A, Cheron G, Orr HT,

770   Pandolfo M, Schiffmann SN (2011) Aminopyridines correct early dysfunction and delay

771   neurodegeneration in a mouse model of spinocerebellar ataxia type 1. J Neurosci 31:11795-

772   11807.

773   Huang S, Uusisaari MY (2013) Physiological temperature during brain slicing enhances the quality

774   of acute slice preparations. Front Cell Neurosci 7:48.

775   Indriati DW, Kamasawa N, Matsui K, Meredith AL, Watanabe M, Shigemoto R (2013)

776   Quantitative localization of Cav2.1 (P/Q-type) voltage-dependent calcium channels in

777   Purkinje cells: somatodendritic gradient and distinct somatic coclustering with calcium-

778   activated potassium channels. J Neurosci 33:3668-3678.

779   Ito M (2013) Error detection and representation in the olivo-cerebellar system. Front Neural
780   Circuits 7:1.

781   Jellinger K (1973) Hypertrophy of the inferior olives. Report on 29 cases. Z Neurol 205:153-174.

782   Kaufmann WA, Ferraguti F, Fukazawa Y, Kasugai Y, Shigemoto R, Laake P, Sexton JA, Ruth P,
783   Wietzorrek G, Knaus HG, Storm JF, Ottersen OP (2009) Large-conductance calcium-
784   activated potassium channels in purkinje cell plasma membranes are clustered at sites of
785   hypolemmal microdomains. J Comp Neurol 515:215-230.

786   Kim D, Langmead B, Salzberg SL (2015) HISAT: a fast spliced aligner with low memory
787   requirements. Nat Methods 12:357-360.

788   Koeppen AH (2005) The pathogenesis of spinocerebellar ataxia. Cerebellum 4:62-73.

789   Koeppen AH (2018) The neuropathology of the adult cerebellum. Handb Clin Neurol 154:129-
790   149.

791   Koeppen AH, Ramirez RL, Bjork ST, Bauer P, Feustel PJ (2013) The reciprocal cerebellar
792   circuitry in human hereditary ataxia. Cerebellum 12:493-503.

793   Konigsmark BW, Weiner LP (1970) The olivopontocerebellar atrophies: a review. Medicine
794   (Baltimore) 49:227-241.

795   Lam YC, Bowman AB, Jafar-Nejad P, Lim J, Richman R, Fryer JD, Hyun ED, Duvick LA, Orr
796   HT, Botas J, Zoghbi HY (2006) ATAXIN-1 interacts with the repressor Capicua in its
797   native complex to cause SCA1 neuropathology. Cell 127:1335-1347.

798   Lang EJ, Sugihara I, Llinas R (1996) GABAergic modulation of complex spike activity by the
799   cerebellar nucleoolivary pathway in rat. J Neurophysiol 76:255-275.

800   Lang EJ, Sugihara I, Llinas R (1997) Differential roles of apamin- and charybdotoxin-sensitive

801   K+ conductances in the generation of inferior olive rhythmicity in vivo. J Neurosci

802   17:2825-2838.

803   Lang EJ, Apps R, Bengtsson F, Cerminara NL, De Zeeuw CI, Ebner TJ, Heck DH, Jaeger D,

804   Jorntell H, Kawato M, Otis TS, Ozyildirim O, Popa LS, Reeves AM, Schweighofer N,

805   Sugihara I, Xiao J (2017) The Roles of the Olivocerebellar Pathway in Motor Learning and

806   Motor Control. A Consensus Paper. Cerebellum 16:230-252.

807   Lefler Y, Yarom Y, Uusisaari MY (2014) Cerebellar inhibitory input to the inferior olive decreases

808   electrical coupling and blocks subthreshold oscillations. Neuron 81:1389-1400.

809   Lein ES et al. (2007) Genome-wide atlas of gene expression in the adult mouse brain. Nature

810   445:168-176. Available from http://mouse.brain-map.org.

811   Liao Y, Smyth GK, Shi W (2014) featureCounts: an efficient general purpose program for

812   assigning sequence reads to genomic features. Bioinformatics 30:923-930.

813   Lin X, Antalffy B, Kang D, Orr HT, Zoghbi HY (2000) Polyglutamine expansion down-regulates

814   specific neuronal genes before pathologic changes in SCA1. Nat Neurosci 3:157-163.

815   Llinas R, Yarom Y (1981a) Electrophysiology of mammalian inferior olivary neurones in vitro.

816   Different types of voltage-dependent ionic conductances. J Physiol 315:549-567.

817   Llinas R, Yarom Y (1981b) Properties and distribution of ionic conductances generating

818   electroresponsiveness of mammalian inferior olivary neurones in vitro. J Physiol 315:569-

819   584.

820   Llinas R, Yarom Y (1986) Oscillatory properties of guinea-pig inferior olivary neurones and their

821   pharmacological modulation: an in vitro study. J Physiol 376:163-182.

822   Llinas RR (2009) Inferior olive oscillation as the temporal basis for motricity and oscillatory reset

823   as the basis for motor error correction. Neuroscience 162:797-804.

824   Llinas RR (2013) The olivo-cerebellar system: a key to understanding the functional significance

825   of intrinsic oscillatory brain properties. Front Neural Circuits 7:96.

826   Love MI, Huber W, Anders S (2014) Moderated estimation of fold change and dispersion for

827   RNA-seq data with DESeq2. Genome Biol 15:550.

828   Niewiadomska-Cimicka A, Hache A, Trottier Y (2020) Gene Deregulation and Underlying

829   Mechanisms in Spinocerebellar Ataxias With Polyglutamine Expansion. Front Neurosci

830   14:571.

831   Ogut E, Armagan K, Tufekci D (2023) The Guillain-Mollaret triangle: a key player in motor

832   coordination and control with implications for neurological disorders. Neurosurg Rev

833   46:181.

834   Pandey P, Westbroek EM, Gooderham PA, Steinberg GK (2013) Cavernous malformation of

835   brainstem, thalamus, and basal ganglia: a series of 176 patients. Neurosurgery 72:573-589;

836   discussion 588-579.

837   Paulson HL (2009) The spinocerebellar ataxias. J Neuroophthalmol 29:227-237.

838   Peng H, Ruan Z, Long F, Simpson JH, Myers EW (2010) V3D enables real-time 3D visualization

839   and quantitative analysis of large-scale biological image data sets. Nat Biotechnol 28:348-

840   353.

841   Peng H, Bria A, Zhou Z, Iannello G, Long F (2014a) Extensible visualization and analysis for

842   multidimensional images using Vaa3D. Nat Protoc 9:193-208.

843   Peng H, Tang J, Xiao H, Bria A, Zhou J, Butler V, Zhou Z, Gonzalez-Bellido PT, Oh SW, Chen

844   J, Mitra A, Tsien RW, Zeng H, Ascoli GA, Iannello G, Hawrylycz M, Myers E, Long F

845   (2014b) Virtual finger boosts three-dimensional imaging and microsurgery as well as

846   terabyte volume image visualization and analysis. Nat Commun 5:4342.

847   Rousseaux MWC et al. (2018) ATXN1-CIC Complex Is the Primary Driver of Cerebellar

848   Pathology in Spinocerebellar Ataxia Type 1 through a Gain-of-Function Mechanism.

849   Neuron 97:1235-1243 e1235.

850   Rub U, Schols L, Paulson H, Auburger G, Kermer P, Jen JC, Seidel K, Korf HW, Deller T (2013)

851   Clinical features, neurogenetics and neuropathology of the polyglutamine spinocerebellar

852   ataxias type 1, 2, 3, 6 and 7. Prog Neurobiol 104:38-66.

853   Ruigrok TJ, de Zeeuw CI, Voogd J (1990) Hypertrophy of inferior olivary neurons: a degenerative,

854   regenerative or plasticity phenomenon. Eur J Morphol 28:224-239.

855   Sabat S, Mannering N, Agarwal A (2016) Hypertrophic olivary degeneration: Case series and

856   review of literature. J Neurol Sci 370:180-186.

857   Schwaller B, Meyer M, Schiffmann S (2002) 'New' functions for 'old' proteins: the role of the

858   calcium-binding proteins calbindin D-28k, calretinin and parvalbumin, in cerebellar

859   physiology. Studies with knockout mice. Cerebellum 1:241-258.

860   Scott SSO, Pedroso JL, Barsottini OGP, Franca-Junior MC, Braga-Neto P (2020) Natural history

861   and epidemiology of the spinocerebellar ataxias: Insights from the first description to

862   nowadays. J Neurol Sci 417:117082.

863   Seidel K, Siswanto S, Brunt ER, den Dunnen W, Korf HW, Rub U (2012) Brain pathology of

864   spinocerebellar ataxias. Acta Neuropathol 124:1-21.

865   Smets G, Lambert J, Tijssen M, Mai C, Decramer T, Vandenberghe W, Van Loon J, Demaerel P

866   (2017) The dentato-rubro-olivary pathway revisited: New MR imaging observations

867   regarding hypertrophic olivary degeneration. Clin Anat 30:543-549.

868   Streng ML, Popa LS, Ebner TJ (2018) Complex Spike Wars: a New Hope. Cerebellum 17:735-
869   746.

870   Switonski PM, Szlachcic WJ, Krzyzosiak WJ, Figiel M (2015) A new humanized ataxin-3 knock-
871   in mouse model combines the genetic features, pathogenesis of neurons and glia and late
872   disease onset of SCA3/MJD. Neurobiol Dis 73:174-188.

873   Tilikete C, Desestret V (2017) Hypertrophic Olivary Degeneration and Palatal or Oculopalatal
874   Tremor. Front Neurol 8:302.

875   Vig PJ, Subramony SH, Burright EN, Fratkin JD, McDaniel DO, Desaiah D, Qin Z (1998)
876   Reduced immunoreactivity to calcium-binding proteins in Purkinje cells precedes onset of
877   ataxia in spinocerebellar ataxia-1 transgenic mice. Neurology 50:106-113.

878   Vrieler N, Loyola S, Yarden-Rabinowitz Y, Hoogendorp J, Medvedev N, Hoogland TM, De
879   Zeeuw CI, De Schutter E, Yarom Y, Negrello M, Torben-Nielsen B, Uusisaari MY (2019)
880   Variability and directionality of inferior olive neuron dendrites revealed by detailed 3D
881   characterization of an extensive morphological library. Brain Struct Funct 224:1677-1695.

882   Walter JT, Alvina K, Womack MD, Chevez C, Khodakhah K (2006) Decreases in the precision of
883   Purkinje cell pacemaking cause cerebellar dysfunction and ataxia. Nat Neurosci 9:389-397.

884   Wang H, Wang Y, Wang R, Li Y, Wang P, Li J, Du J (2019) Hypertrophic olivary degeneration:
885   A comprehensive review focusing on etiology. Brain Res 1718:53-63.

886   Warnaar P, Couto J, Negrello M, Junker M, Smilgin A, Ignashchenkova A, Giugliano M, Thier P,
887   De Schutter E (2015) Duration of Purkinje cell complex spikes increases with their firing
888   frequency. Front Cell Neurosci 9:122.

889   Watase K, Weeber EJ, Xu B, Antalffy B, Yuva-Paylor L, Hashimoto K, Kano M, Atkinson R, Sun
890   Y, Armstrong DL, Sweatt JD, Orr HT, Paylor R, Zoghbi HY (2002) A long CAG repeat in

891   the mouse Sca1 locus replicates SCA1 features and reveals the impact of protein solubility

892   on selective neurodegeneration. Neuron 34:905-919.

893   Womack MD, Chevez C, Khodakhah K (2004) Calcium-activated potassium channels are

894   selectively coupled to P/Q-type calcium channels in cerebellar Purkinje neurons. J

895   Neurosci 24:8818-8822.

896   Yoshii F, Tomiyasu H, Watanabe R, Ryo M (2017) MRI Signal Abnormalities of the Inferior

897   Olivary Nuclei in Spinocerebellar Ataxia Type 2. Case Rep Neurol 9:267-271.

898   Yu Y, Fu Y, Watson C (2014) The inferior olive of the C57BL/6J mouse: a chemoarchitectonic

899   study. Anat Rec (Hoboken) 297:289-300.

900   Zanjani H, Herrup K, Mariani J (2004) Cell number in the inferior olive of nervous and leaner

901   mutant mice. J Neurogenet 18:327-339.

902

903

904

Figure 1

Morrison et al., submitted 2023
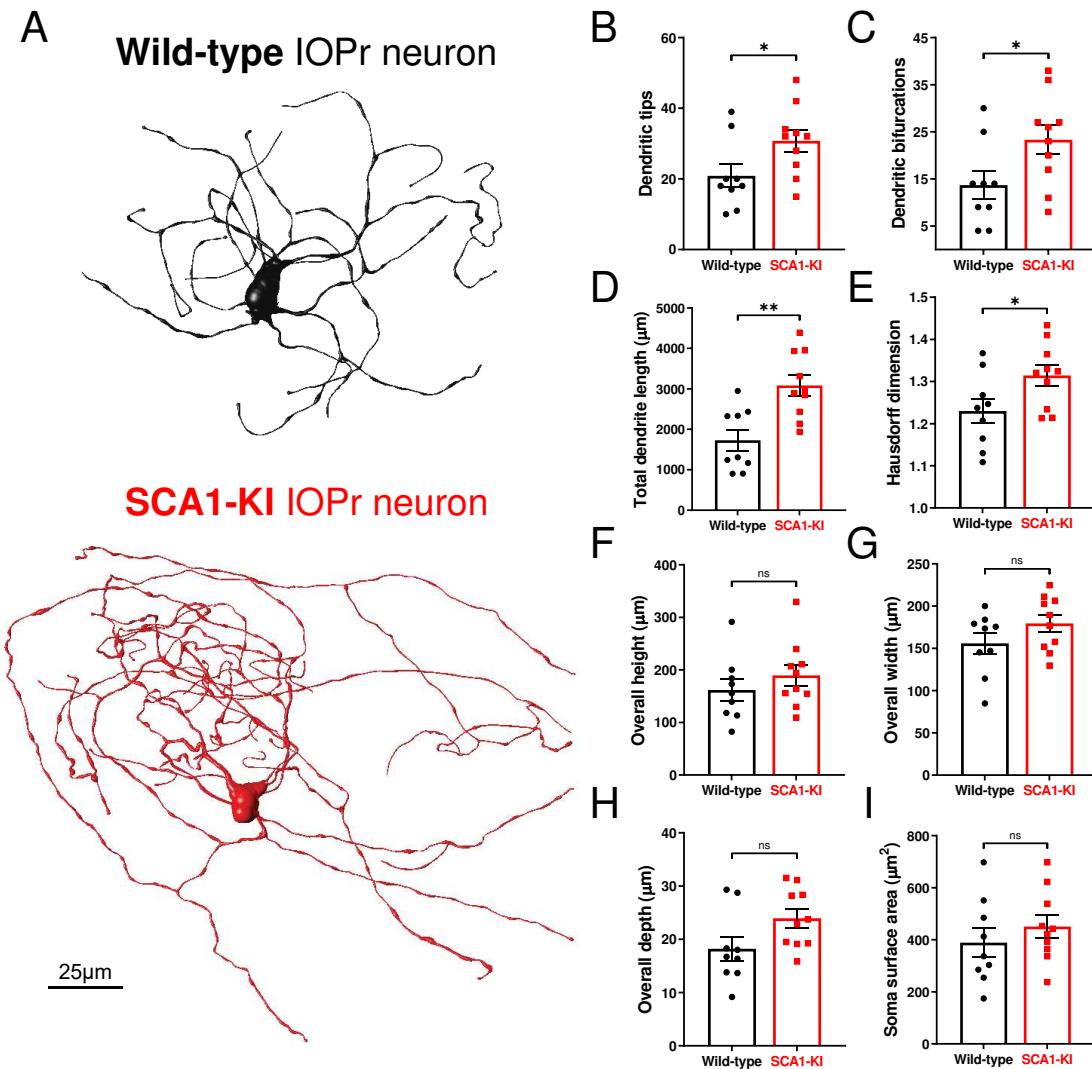
Figure 1. IOPr neuron dendritic arbors are hypertrophic in SCA1-KI mice

(A) Representative morphological reconstructions of dye-filled IO neurons in wild-type (top) and SCA1-KI (bottom) mice at 14 weeks of age (an early symptomatic timepoint). **(B-I)** The dendritic arbors of SCA1-KI IO neurons are larger and more complex than wild-type controls. SCA1-KI IO neurons exhibit a greater number of dendritic tips **(B)** and dendritic bifurcations **(C)**, as well as a marked increase in total dendritic length **(D)** and Hausdorff dimension **(E)** (a three-dimensional measure of object complexity). The overall span of IO neurons, shown as height **(F)**, width **(G)**, and depth **(H)**, is largely unchanged between the two genotypes. No change in IO soma size (measured by surface area) was detected between the two genotypes **(I)**. Data are expressed as mean ± SEM. Statistical significance derived by unpaired t-test with Welch's correction, * = $P < 0.05$, ** = $P < 0.01$, ns = not significant. $N_{wild-type}$ = 9 cells from 7 mice, $N_{SCA1-KI}$ = 10 cells from 7 mice.

Figure 2   Morrison et al., submitted 2023

A EARLY SYMPTOMATIC TIMEPOINT (14 weeks)

44
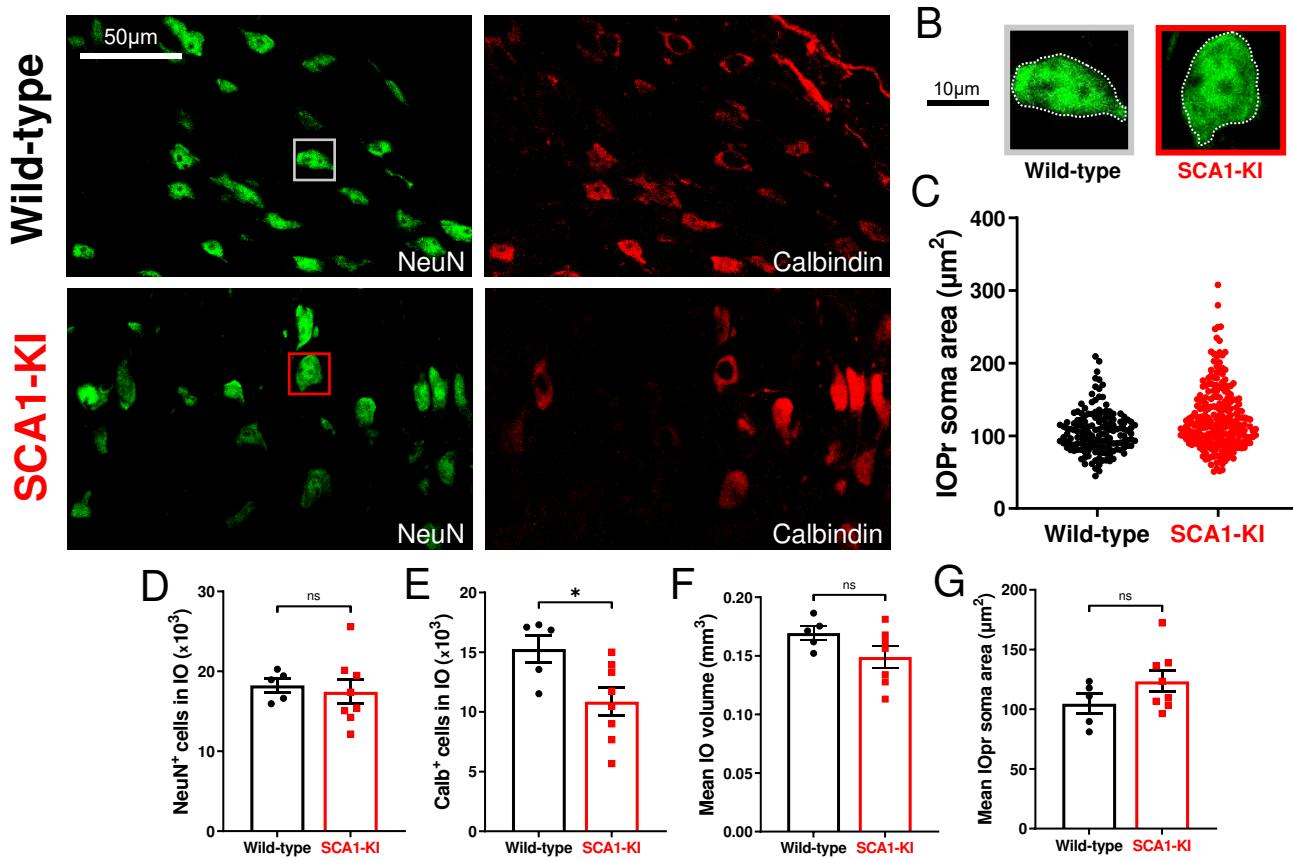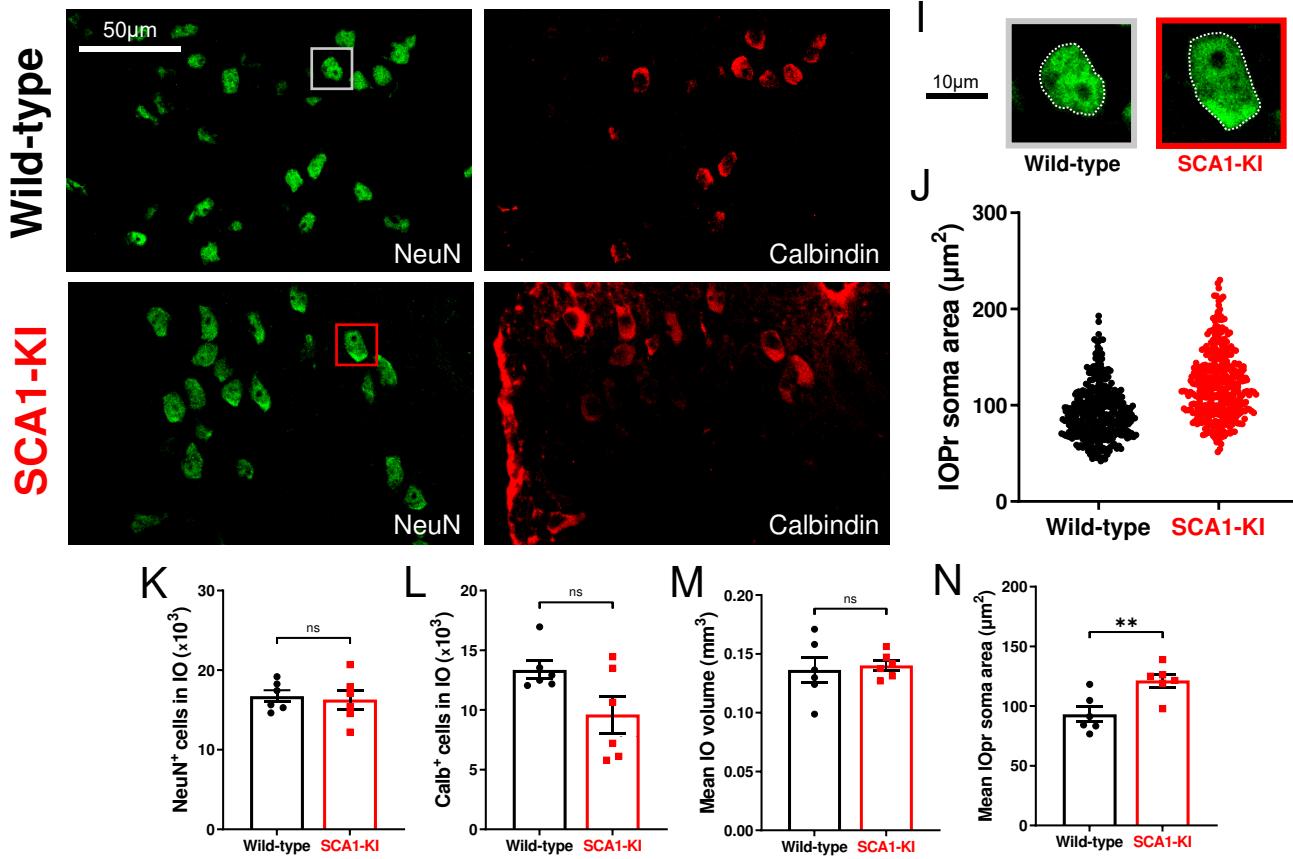
Figure 2. IO neurons in SCA1-KI mice exhibit somatic hypertrophy and degeneration

(A) Coronal histological sections showing IOPr neurons in wild-type (top) and SCA1-KI (bottom) mice at an early symptomatic timepoint of 14 weeks. Sections have been stained for NeuN (green) and Calbindin (red). **(B)** Inset showing representative IOPr cells of each genotype. **(C, G)** IOPr neuron soma size was estimated by measuring the area of the soma in ~200 cells per genotype. No change in IOPr soma size in SCA1-KI mice is evident at the 14 week timepoint. **(D-F)** Quantification of unbiased stereological analysis, providing an estimate of both total cell number and gross volume for the entire IO. At 14 weeks, degeneration is already apparent in the SCA1-KI IO, shown by loss of calbindin signal. **(H)** Coronal histological sections showing principal IO in wild-type (top) and SCA1-KI (bottom) mice at a late symptomatic timepoint of 30 weeks. Sections have been stained for NeuN (green) and Calbindin (red). **(I)** Inset showing representative IOPr cells of each genotype. **(J, N)** IOPr neuron soma size was estimated by measuring the area of the soma in ~400 cells per genotype. At the 30 week timepoint, SCA1-KI IOPr neurons exhibit a highly significant increase in soma size **(J)**, with a shift in the entire distribution of neurons towards a larger size **(N)**. **(K-M)** Quantification of unbiased stereological analysis reveals an even greater loss of calbindin signal at 30 weeks **(K-M)**, indicating a more severe degenerative state. Data are expressed as mean ± SEM. Statistical significance derived by unpaired t-test with Welch's correction, $*$ = $P < 0.05$, $**$ = $P < 0.01$, ns = not significant. 14 weeks: $N_{wild-type}$ = 5 mice, $N_{SCA1-KI}$ = 8 mice; 30 weeks: $N_{wild-type}$ = 6 mice, $N_{SCA1-KI}$ = 6 mice.

Figure 3

EARLY SYMPTOMATIC TIMEPOINT (14 weeks)
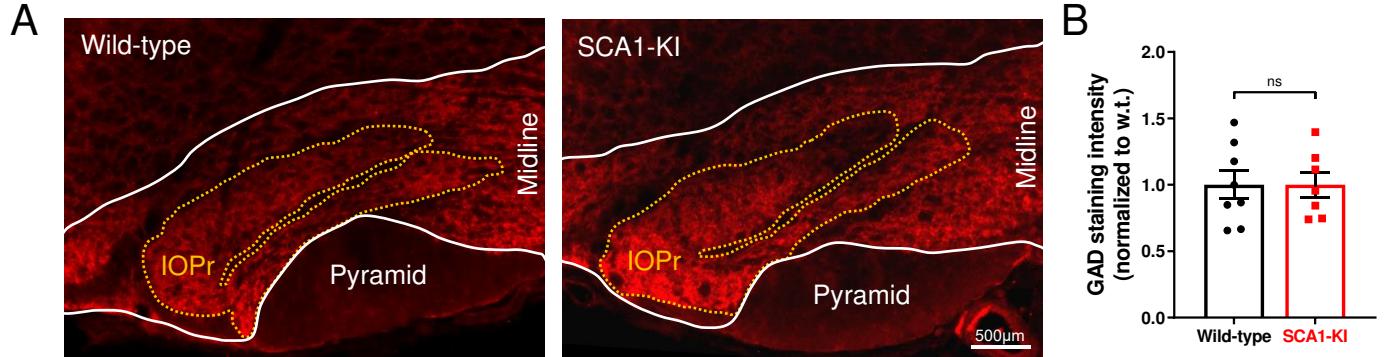
## LATE SYMPTOMATIC TIMEPOINT (30 weeks)
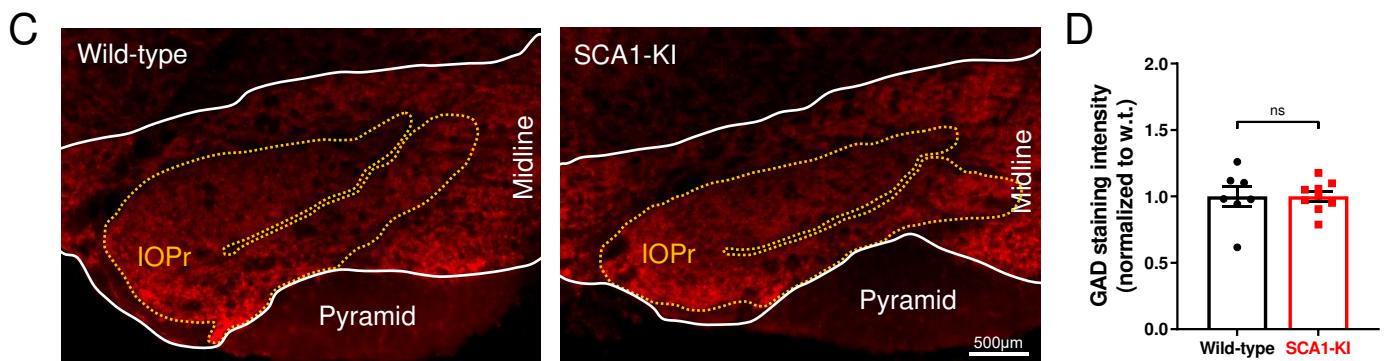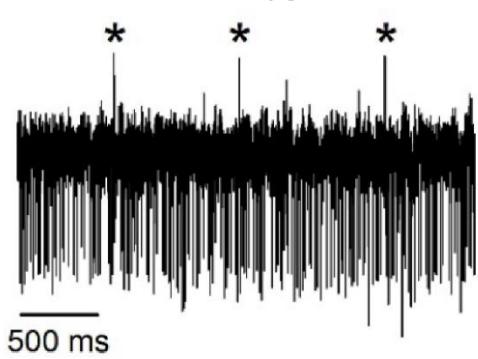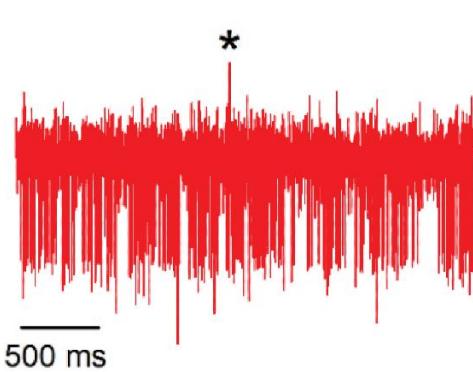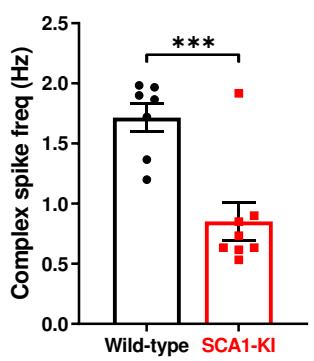
Figure 3. Inhibitory synaptic inputs to the IO remain intact in SCA1-KI mice

(A) Coronal histological sections showing the IOPr in wild-type (left) and SCA1-KI (right) mice at an early symptomatic timepoint of 14 weeks. Sections have been stained for glutamate decarboxylase (GAD), a marker of GABAergic terminals (red). **(B)** Quantification of staining reveals that GAD signal is retained in the SCA1-KI IO at 14 weeks. **(C)** Coronal histological sections showing GAD staining in the principal IO at a late symptomatic timepoint of 30 weeks. **(D)** Quantification of staining reveals that GAD signal is also retained in the SCA1-KI IO at 30 weeks. **(E)** Representative traces of *in-vivo* cerebellar spiking patterns in head-fixed, awake mice at 14 weeks. Complex spikes (generated by IO neurons) are indicated with asterisks (*). **(F)** Complex spike frequency is reduced in SCA1-KI cerebella, suggesting that IO neurons *in-vivo* are not disinhibited by loss of inhibitory synaptic input. Data are expressed as mean ± SEM. Statistical significance derived by unpaired *t*-test with Welch's correction, *** = $P < 0.001$, ns = not significant. **(A-D)** 14 weeks: $N_{wild-type} = 8$ mice, $N_{SCA1-KI} = 7$ mice; 30 weeks: $N_{wild-type} = 7$ mice, $N_{SCA1-KI} = 9$ mice. **(E,F)** $N_{wild-type} = 7$ mice, $N_{SCA1-KI} = 8$ mice.

Figure 4   Morrison et al., submitted 2023

A **LATE SYMPTOMATIC TIMEPOINT (14 weeks)**
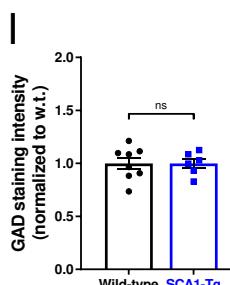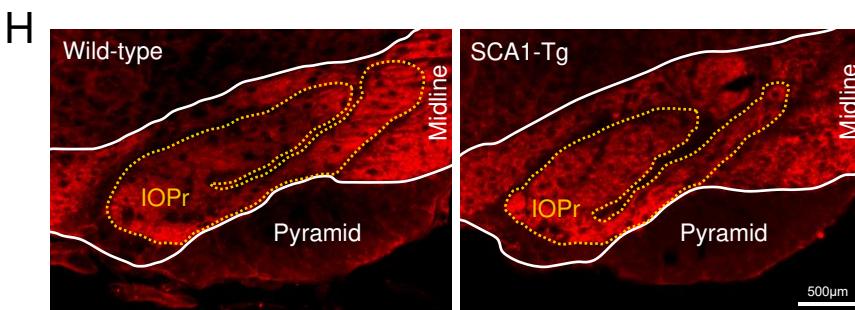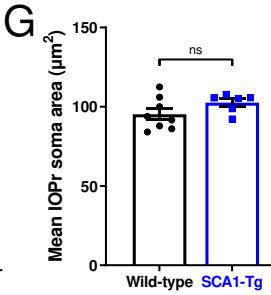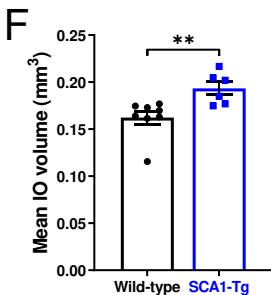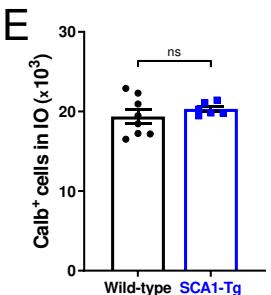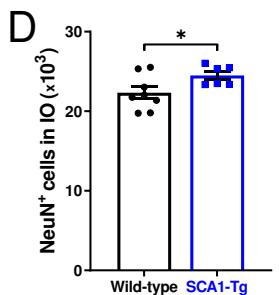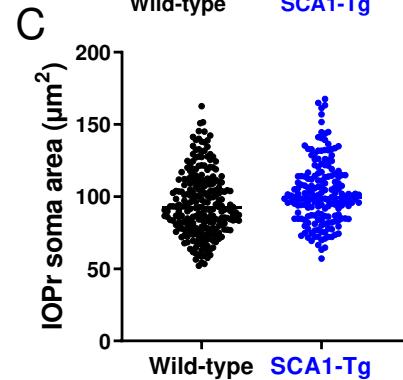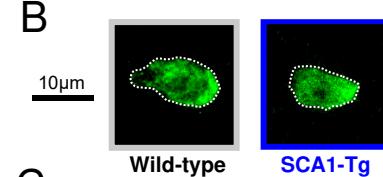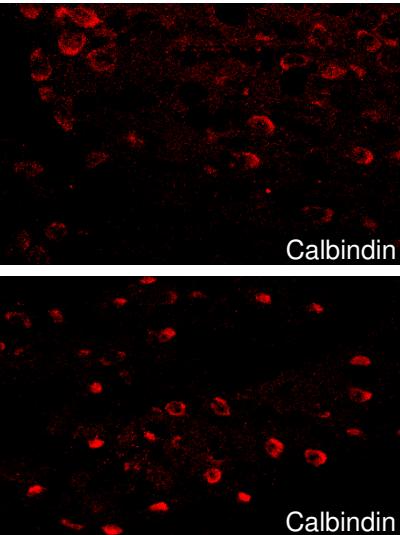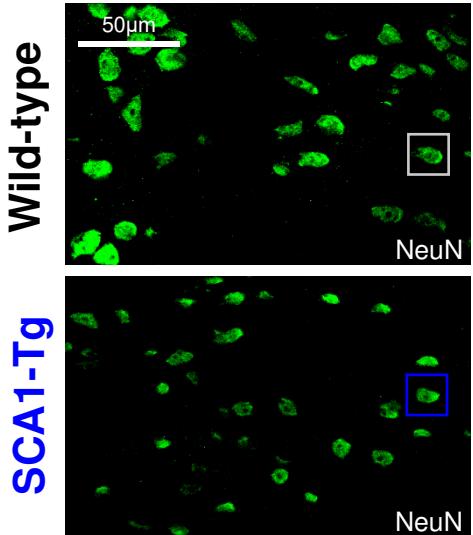
Figure 4. IO neuron size and viability is retained in a Purkinje cell-specific mouse model of SCA1

(A) Coronal histological sections showing IOPr neurons in wild-type (top) and SCA1-Tg (bottom) mice at 14 weeks. Unlike SCA1-KI mice, SCA1-Tg mice express mutant *ATXN1* solely in Purkinje cells of the cerebellum (i.e., not in the IO). These mice have a more severe phenotype, making 14 weeks of age a late symptomatic timepoint. Sections have been stained for NeuN (green) and Calbindin (red). **(B)** Inset showing representative IOPr cells of each genotype. **(C, G)** IOPr neuron soma size was estimated by measuring the area of the soma in ~200 cells per genotype. No change in IOPr soma size in SCA1-Tg mice is evident at this timepoint. **(D-F)** Quantification of unbiased stereological analysis, providing an estimate of both total cell number and gross volume for the entire IO. At 14 weeks, degeneration is not apparent in the SCA1-Tg IO. **(H)** Coronal histological sections showing principal IO in wild-type (left) and SCA1-Tg (right) mice at 14 weeks. Sections have been stained for glutamate decarboxylase (GAD), a marker of GABAergic terminals (red). **(I)** Quantification of staining reveals that GAD signal is retained in the SCA1-Tg IO at 14 weeks, indicating no loss of inhibitory synaptic input in these mice. Data are expressed as mean ± SEM. Statistical significance derived by unpaired *t*-test with Welch's correction, * = $P < 0.05$, ns = not significant. **(A-G)** $N_{wild-type}$ = 8 mice, $N_{SCA1-Tg}$ = 6 mice **(H,I)** $N_{wild-type}$ = 8 mice, $N_{SCA1-Tg}$ = 6 mice.

Figure 5

Morrison et al., submitted 2023

50
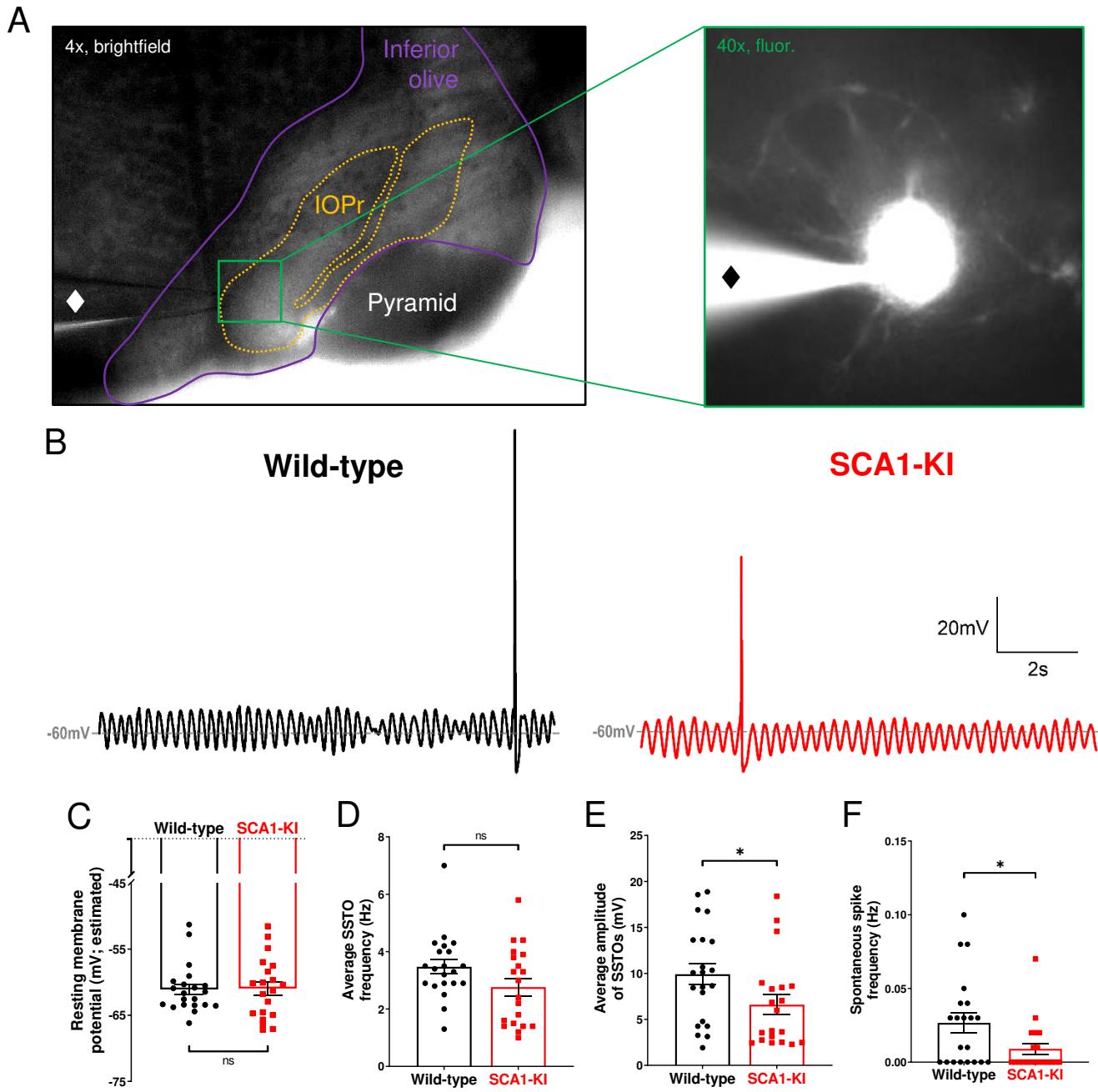
Figure 5. Spontaneous activity in SCA1-KI IOPr neurons is largely unchanged

(A) Images demonstrating whole-cell patch-clamp electrophysiology on IO neurons in coronal brainstem slices at 4x magnification (left) and 40x magnification (right). Internal solution included a small amount of fluorescent dye that filled cells while recording, allowing for the single-cell morphological analysis shown in **Fig. 1**. A ♦ symbol marks the recording electrode. **(B)** Representative traces of spontaneous activity in IOPr neurons from wild-type (left) and SCA1-KI (right) mice at an early symptomatic timepoint of 14 weeks. The presence of spontaneous subthreshold oscillations (SSTOs) was used as confirmation of cell type when recording. **(C-F)** Quantification of various electrophysiological properties show few differences between SCA1-KI and wild-type IOPr neurons at rest. There was no apparent change in resting membrane potential[‡] **(C)** or SSTO frequency **(D)** between genotypes, though SCA1-KI IOPr neurons did exhibit diminished SSTO amplitude **(E)** and spontaneous spike generation **(F)**. Data are expressed as mean ± SEM. Statistical significance derived by unpaired *t*-test with Welch's correction, * = $P < 0.05$, ns = not significant. [‡]Due to the persistence of SSTOs, the average membrane potential across 10 s or recording was used as an estimate of resting membrane potential. $N_{wild-type}$ = 21 cells from 15 mice, $N_{SCA1-KI}$ = 20 cells from 13 mice.

Figure 6

Morrison et al., submitted 2023
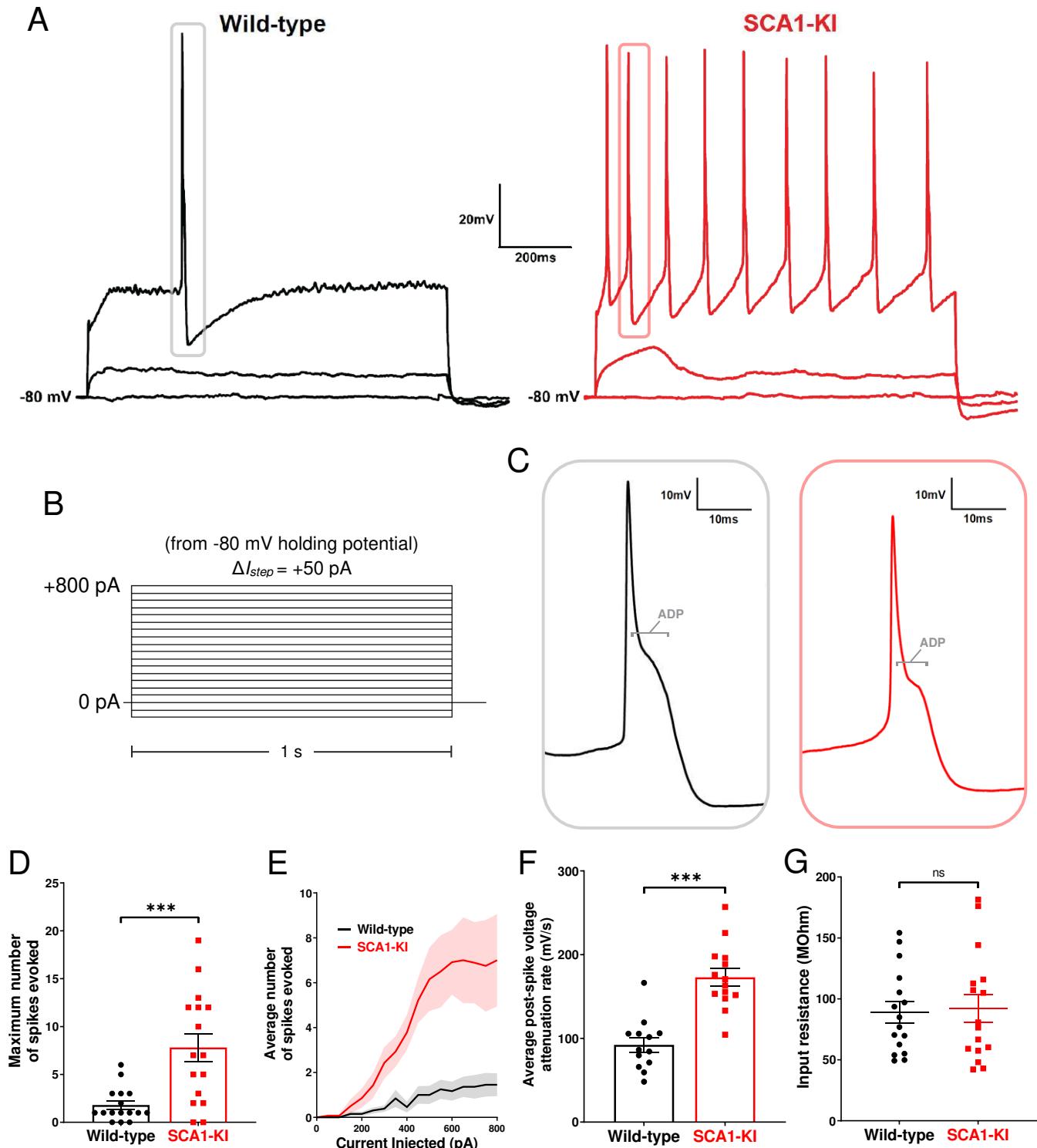
Figure 6. IOPr neurons in SCA1-KI mice are hyperexcitable

(A) Representative traces of evoked activity in IO neurons from wild-type (left) and SCA1-KI (right) mice at an early symptomatic timepoint (14wks). Traces shown for each group are 0 pA injected (bottom trace), +200 pA injected (middle trace), and +550 pA injected (top trace). **(B)** From a holding potential of -80 mV, a range of 0-800 pA depolarizing currents were injected in +50 pA, 1 second steps. Recordings were performed in current clamp mode. **(C)** Inset of representative evoked spikes at a higher timescale resolution reveal a long afterdepolarization (ADP) "hump," a characteristic feature of IOPr neurons. **(D)** Unlike IO neurons in wild-type mice, IO neurons in SCA1-KI mice are able to sustain a spike train. **(E)** Input-output curve of average spikes produced in IO neurons of each genotype. Number of spikes rose steadily with current injection in SCA1-KI IO neurons, while wild-type IO neurons rarely exhibited spiking in the range depicted (+0-800 pA injected). **(F)** The rate at which membrane potential recovered back to baseline from its minimum value post-spike was significantly higher in SCA1-KI IOPr neurons, allowing these cells to fire repetitively. **(G)** Input resistance of IO neurons is unchanged in SCA1-KI mice, demonstrating that this hyperexcitability phenotype is not a product of any change in voltage generated per injected current step. Data are expressed as mean ± SEM. Statistical significance derived by unpaired t-test with Welch's correction, *** = $P < 0.001$, ns = not significant. **(D,E,G)** $N_{wild\text{-}type}$ = 16 cells from 14 mice, $N_{SCA1\text{-}KI}$ = 16 cells from 11 mice **(F)** Non-firing cells removed, so $N_{wild\text{-}type}$ = 13 cells from 12 mice, $N_{SCA1\text{-}KI}$ = 14 cells from 9 mice.

Figure 7
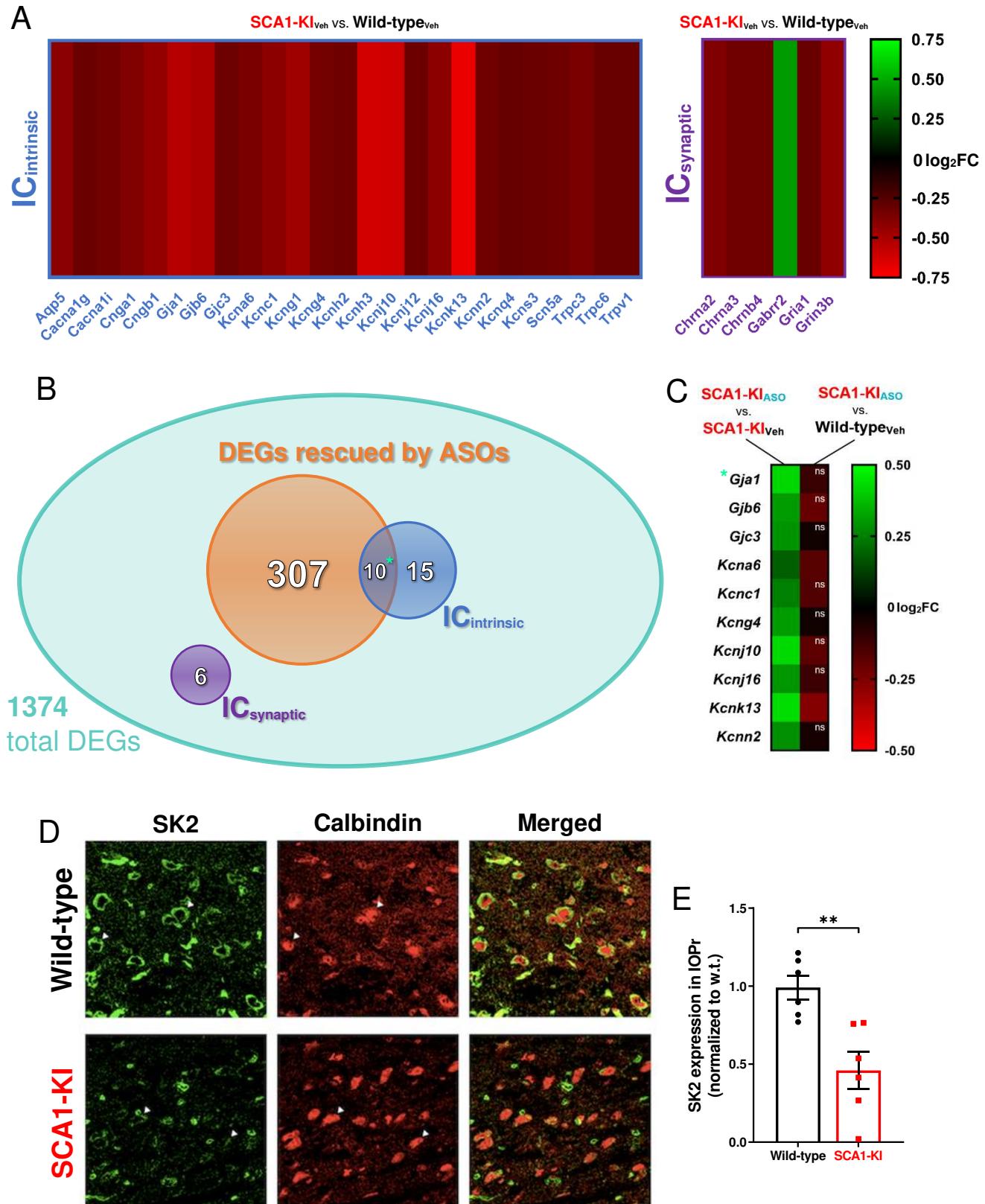
Figure 7. Ion channel expression is disrupted in the SCA1-KI medulla

(A) Transcriptomic analysis of whole medulla from SCA1-KI and wild-type mice at 28 weeks reveal that 31 ion channel genes are differentially expressed. Of these, 25 influence excitability intrinsically ($IC_{intrinsic}$), while 6 influence excitability synaptically ($IC_{synaptic}$). **(B)** Downregulation of *Atxn1* expression by antisense oligonucleotides (ASOs) ameliorates brainstem phenotypes in SCA1-KI mice. Of the 1374 differentially expressed genes (DEGs) in the SCA1-KI medulla, 317 DEGs were significantly rescued by ASO treatment (and, therefore, are more likely to be responsible for the observed phenotypic rescue). Within this cohort, $IC_{intrinsic}$ genes were significantly enriched. **(C)** Heatmap showing differential expression of the 10 $IC_{intrinsic}$ DEGs between treatment groups. These ion channel genes exhibited a significant increase in expression after ASO treatment (left), with the majority of them rising to wild-type levels (right). **(D)** In order to examine how decreases in medullary ion channel transcripts may result in a loss of channels in the IOPr, immunostaining for the small-conductance potassium channel SK2 was performed. Coronal histological sections of the IOPr in wild-type (top) and SCA1-KI (bottom) mice at 14 weeks (an early symptomatic timepoint) are shown. Sections have been stained for SK2 (green) and calbindin (red). **(E)** Quantification of immunostaining reveals a significant loss of SK2 channels on the membrane of SCA1-KI IOPr neurons. Data are expressed as mean ± SEM. Statistical significance derived by Fischer's exact test (enrichment analyses) or unpaired *t*-test with Welch's correction (all other comparisons), ** = $P < 0.01$, ns = not significant. **(A-C)** $N_{wild\text{-}type,\ Vehicle}$ = 8 mice, $N_{SCA1\text{-}KI,\ Vehicle}$ = 8 mice, $N_{SCA1\text{-}KI,\ ASO}$ = 7 mice. **(D, E)** $N_{wild\text{-}type}$ = 6 mice, $N_{SCA1\text{-}KI}$ = 6 mice.

Figure 8

IOPr neuron spike trains from -80 mV
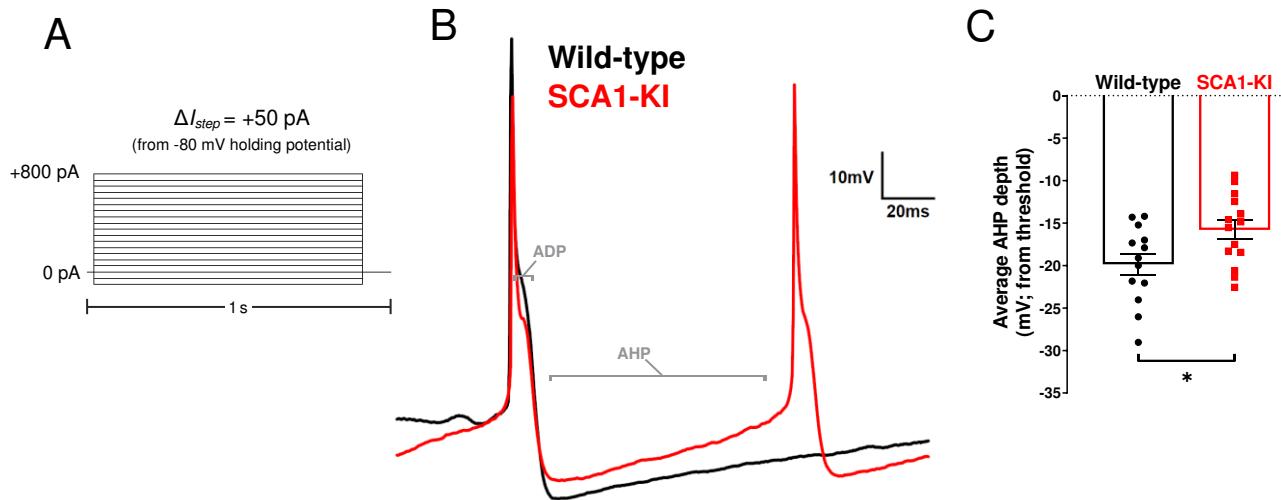

IOPr neuron single spikes from -60 mV

56
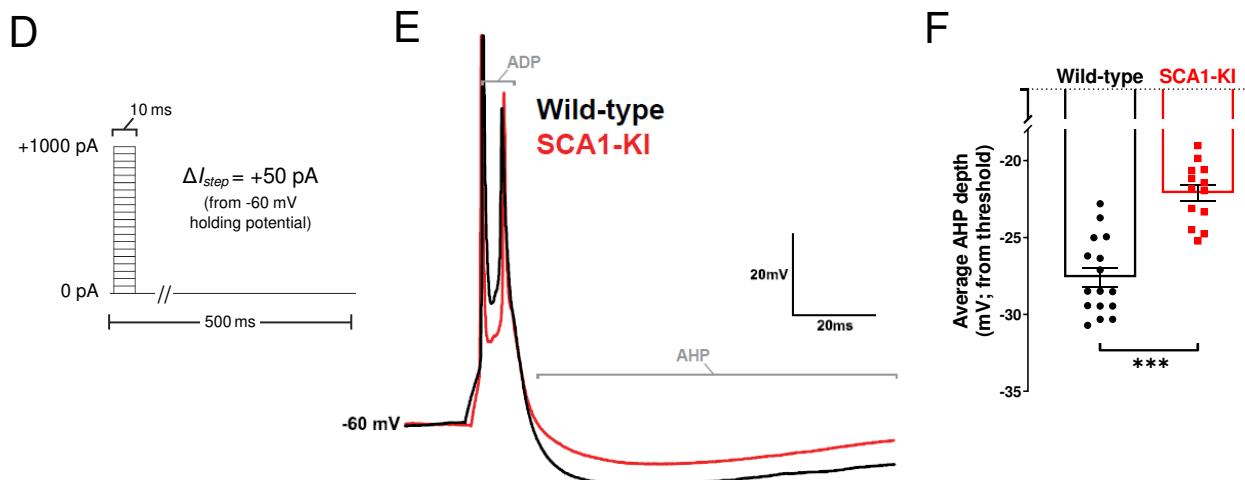
Figure 8. Spike afterhyperpolarization is diminished in SCA1-KI IOPr neurons

(A) In order to assess the functional relevance of ion channel loss in SCA1-KI IOPr neurons, spike trains were generated by injecting increasing levels of current from -80 mV (a holding potential at which active conductances are minimal in the IO). **(B)** Representative traces of spikes generated by injecting +450 pA current in IOPr neurons of wild-type and SCA1-KI mice at 14 weeks. **(C)** Quantification of AHP depth (measured from each spike's threshold), demonstrating that SCA1-KI IOPr spikes during spike trains exhibit a shallower AHP compared to wild-type. **(D)** In order to determine if this AHP loss can also occur at rest, single spikes were generated by injecting increasing levels of current from -60 mV (a holding potential close to resting V_m). Because the amount of current needed to generate a single spike varied between cells, the first spike that exhibited an ADP was used for comparisons. **(E)** Representative traces of evoked activity in IOPr neurons in wild-type and SCA1-KI mice at 14 weeks are overlaid. **(F)** Quantification of AHP depth (measured from each spike's threshold), demonstrating that SCA1-KI IO neuron spikes from rest also exhibit a shallower AHP compared to wild-type. Data are expressed as mean ± SEM. Statistical significance derived by unpaired *t*-test with Welch's correction, * = $P < 0.05$, *** = $P < 0.001$. **(A-C)** $N_{wild-type}$ = 13 cells from 12 mice, $N_{SCA1-KI}$ = 14 cells from 9 mice. **(D-F)** $N_{wild-type}$ = 16 cells from 14 mice, $N_{SCA1-KI}$ = 13 cells from 9 mice.